doi:10.26443/seismica.v5i2.1539

SEISMICA

Paleoseismic evidence for surface rupturing earthquakes on the West Caspian Fault (Azerbaijan): an active right lateral strike slip fault zone in an over-pressured sedimentary basin

Neill Marshall *[1,2,3], **Ibrahim Guliyev** [4], **Gurban Yetirmishli** [5], **Rauf Muradov** [5], **Sabina Kazimova** [5], **Ilyas Kazimov** [5], **Ian Pierce** [1], **Ed Rhodes**[6,7], **Richard T. Walker**[1], **Rashid Javanshir**[4,5], **Ben Johnson**[1], **Gregory De Pascale** [8]

[1]COMET, Department of Earth Sciences, Oxford University, Oxford, OX1 3AN, UK, [2]Royal Observatory Belgium, Brussels, Belgium 1180, [3]University of Liège, Liège, Belgium, [4]Azerbaijan National Academy of Science, Baku, Azerbaijan, [5]Republican Seismic Survey Center of Azerbaijan National Academy of Science, Baku, Azerbaijan, [6]Department of Geography, University of Sheffield, Sheffield, S10 2TN, UK, [7]Department of Earth, Planetary, and Space Sciences, University of California Los Angeles, Los Angeles, CA 90095-1567, USA, [8]School of Engineering and Natural Sciences, University of Iceland, Reykjavík, Iceland

Author contributions: *Conceptualization*: N. Marshall, I. Pierce and R.T. Walker. *Data Curation*: N. Marshall, I. Pierce, G. De Pascale and E. Rhodes . *Formal Analysis*: N. Marshall. *Funding Acquisition*: R.T. Walker. *Investigation*: N. Marshall. *Methodology*: N. Marshall, I. Pierce, E. Rhodes. *Project Administration*: N. Marshall. *Resources*: N. Marshall, I. Guliyev, R. T. Walker. *Software*: N. Marshall. *Supervision*: N. Marshall, R.T. Walker. *Validation*: N. Marshall, I. Pierce, R.T. Walker. *Visualization*: N. Marshall. *Writing – original draft*: N. Marshall. *Writing – review & editing*: N. Marshall, S. Kazimova, I. Kazimov, I. Pierce, E. Rhodes, R.T. Walker, R. Javanshir, B. Johnson, G. De Pascale, I. Guliyev, G. Yetirmishli, R. Muradov.

Abstract We provide the first geomorphic evidence for active right-lateral strike-slip faulting at the eastern margins of the Greater Caucasus and western margins of the South Caspian Basin. The West Caspian Fault comprises several parallel strands, exhibiting numerous right-lateral stream deflections, following mud volcano alignments. Mud volcanoes occur predominantly at bends and folds along the otherwise strike-slip trace, indicating a structural control on emplacement. Mud volcano distribution and alignments in seismicity allow us to infer a total fault length of ~150 km. We estimate a Holocene slip-rate of 3.9–4.8 mm/yr, based upon a displaced terrace riser of assumed age. Two paleoseismic trenches reveal between five and six surface rupture events over the last 3000 years, and an average recurrence interval of 500–600 years. The events are unevenly spaced in time, with a cluster of 3 events in the last 650 years, and longer intervals earlier. From earthquake scaling relationships we expect rupture of the entire fault length to produce Mw 7.5 events with average slip of 3 m, consistent with the smaller measured lateral offsets. However, a lack of historical earthquakes combined with inferences on fault behaviour within the fluid-rich over-pressured Kura basin sediments lead us to speculate that the ruptures may represent aseismic slip or low-magnitude surface-rupturing earthquakes.

Production Editor:
Andrea Llenos
Handling Editor:
Ake Fagereng
Alexandra Hatem
Copy & Layout Editor:
Hannah F. Mark

Received:
December 19, 2024
Accepted:
July 2, 2026
Published:
August 12, 2026

1 Introduction

Complex deformation occurs in fault boundary zones where multiple tectonic blocks meet. Understanding the behaviour of these complex fault zones is fundamentally important to quantify the rates of relative plate motion and regional seismic hazard. The junction between the Greater Caucasus, South Caspian, and Kura basins is an important example of a complex boundary (Fig. 1). Little is known about the active faulting occurring between the Kura and South Caspian basins and how this zone fits within the regional tectonic framework. Active faulting within and around the Kura basin is likely to play an important role in accommodating motion of the South Caspian Basin, which is believed to be an aseismic block within the Arabia-Eurasia collision zone (Jackson et al., 2002). Active faulting within the Kura basin also poses potential hazards to relatively large populations and important transport and energy infrastructure. However, rapid sedimentation within the Kura basin and multiple transgressions of the nearby Caspian Sea have acted to largely conceal the geomorphic expression of faulting such that both the existence of major fault zones, and descriptions of their kinematic roles, are debated (e.g. Jackson et al., 2002; Vernant et al., 2004; Copley and Jackson, 2006; Reilinger et al., 2006; Kadirov et al., 2012; Gunnels et al., 2020).

A further complexity is the role basin rheology plays in effecting deformation. High rates of sedimentation leading to overpressure, combined with high pore fluid pressures and tectonic compression in Kura basin raises the potential for shallow aseismic deformation.

In this paper we map active fault traces using optical satellite imagery, field observations, published seismicity (Gunnels et al., 2020), and the distribution of mud volcanoes, to confirm north-south right-lateral strike-slip faulting at the eastern margins of the Kura

*Corresponding author: neill.marshall@oma.be

basin. We show results from paleoseismic trenches near Salyan on the West Caspian Fault, determining the first geologic constraints on slip-rate, earthquake recurrence, displacement, and fault geometry (Fig. 1). We then discuss the role of the West Caspian fault zone in the context of the regional tectonics and triple junctions and whether observed active faulting results from seismic or aseismic slip.

2 Geographic and tectonic setting

The active faulting in Azerbaijan and the South-eastern Caucasus is related both to north-south shortening within the Arabian-Eurasian continental collision zone, and to the motion of the South Caspian basin (e.g. Jackson and McKenzie, 1984; Jackson et al., 2002).

2.1 The Kura Basin

The West Caspian Fault zone sits at the eastern margin of the Kura Basin, a depression between the Greater Caucasus mountains to the north and Lesser Caucasus mountains to the south (Fig. 2). The sedimentary thickness of the Kura Basin is thought to be ~15 km (Piip et al., 2012), underlain by a granitic-metamorphic basement (Nadirov et al., 1997).

The Kura Fold and Thrust Belt is believed to be the southward propagation of the Greater Caucasus into the Kura foreland basin, and the centre of shortening in the region, initiated 1.5 Ma (Forte et al., 2009, 2013). Paleoseismic studies show evidence for three surface rupturing earthquakes along the Kura Fold and Thrust Belt in the last 2300 years, and a maximum Holocene dip-slip shortening rate of 8.0 to 8.5 mm/yr (Pierce et al., 2024).

Crustal thickness of the Kura Basin decreases, due to thinning, from west (~60 km) to east (~45 km) where it borders the South Caspian Basin (Mangino and Priestley, 1998). The Kura River flows eastwards through the basin to the Caspian Sea, leading to relatively high sedimentation rates at the present day. In the north, the Kura Fold and Thrust Belt and Greater Caucasus are being actively uplifted by thrust faulting with seismicity focussed on the frontal thrusts (Fig. 2) (Allen et al., 2004; Copley and Jackson, 2006; Gunnels et al., 2020; Jackson et al., 2002; Forte et al., 2009, 2013). GNSS survey data by Kadirov et al. (2012) and Reilinger et al. (2006) shows northward motion of the Kura Basin with respect to Eurasia of 13.2 ± 0.5mm/yr (Fig. 2 & S1).

Most well-constrained earthquakes in the Kura Basin are moderate in magnitude and have depths that exceed 10 km (e.g., Copley and Jackson, 2006; Gunnels et al., 2020; Jackson et al., 2021, 2002; Engdahl et al., 2006). There are few recorded significant historical earthquakes on or near the West Caspian fault zone over the last 2000 years (Shebalin and Leydecker, 1997), apart from one event in the vicinity of Salyan in 1881 with magnitude 4.0 and intensity V. Ambraseys and Melville (2005) report no earthquakes in the Salyan region although there are two earthquakes in Azerbaijan of unknown origin in 1305 and 1436 (Ambraseys and Melville, 2005).

Eastern Azerbaijan has a high concentration of mud volcanoes, distributed both in the Kura basin onshore and the offshore South Caspian Basin (Fig. 2), with mud sourced from the Oligocene Maykop formation, which underlies the ~10 km thickness of sands of the so-called Productive Series (Allen et al., 2002; Mangino and Priestley, 1998; Piip et al., 2012; Abdullayev et al., 2017). Mud volcanism is driven by sediment overpressure and the presence of hydrocarbons, with tectonic compression from the Arabia-Eurasia collision further contributing to elevated pore pressures within the basins (Feyzullayev et al., 2015; Mazzini and Etiope, 2017).

2.2 The South Caspian Basin

The South Caspian Basin (SCB) is bounded to east, south, and west by the actively deforming Kopeh Dagh, Alborz, and Talesh mountain belts, with its northern boundary at the Apsheron ridge (Fig. 1). Receiver function analysis and seismic reflections studies show, from top to bottom, a low-velocity layer 15–20 km thick, then a 10–18 km thick high-velocity basaltic-like layer beneath (Jackson et al., 2002). The 15–20 km low velocity layer is modelled as a series of sedimentary layers with the Miocene basin fill deposits starting at a depth of ~8–9 km (Abdullayev et al., 2017). The Quaternary layers make up the top 3 km of the basin fill (Allen et al., 2002; Abdullayev et al., 2017).

The basin has few recorded earthquakes within its interior and is believed to be an independent block (Jackson et al., 2002; Walker et al., 2021). The SCB moves with a rate of 10.4 ± 1.1 mm/yr in direction 333° ± 5° relative to Eurasia, and 4.8 ± 0.8 mm/yr in direction 236° ± 14° relative to Iran (Copley and Jackson, 2006; Djamour et al., 2010; Jackson et al., 2002; Walker et al., 2021). North of the Apsheron ridge, earthquakes with depths greater than 80 km occur and are thought to be a result of the basement of the South Caspian subducting north beneath Eurasia (Jackson et al., 2002, 2021; Walker et al., 2021). Westward underplating of the SCB beneath the Talesh and Kura basin is also inferred from deep thrust fault earthquakes, to depths of around 40 km (Jackson et al., 2002). The onset of subduction is often assumed to correlate to increased sediment accumulation in the basin at 5.5 Ma (Allen et al., 2002), though analysis of deep seismic lines through the Apsheron ridge and South Caspian instead suggest that the subduction dates earlier, to the Miocene (e.g. Green et al., 2009).

In the east, the relative motion of the SCB relative to Eurasia and Iran is accommodated via conjugate motion on the dextral Main Kopeh Dagh Fault and sinistral Shahrud Fault zone, as shown in Fig. 1, (Dodds et al., 2022; Hollingsworth et al., 2008; Jackson et al., 2002; Walker et al., 2021). Faulting along the southern side of the SCB changes from east to west, with decreasing amounts of left-lateral slip and increasing shortening components as the Alborz ranges curve around the south side of the SCB. GNSS velocities indicate that the Talesh and Kura basin move northwards relative to Eurasia at 10–13 mm/yr. GNSS studies by Kadirov et al. (2012) and Reilinger et al. (2006) show a north-

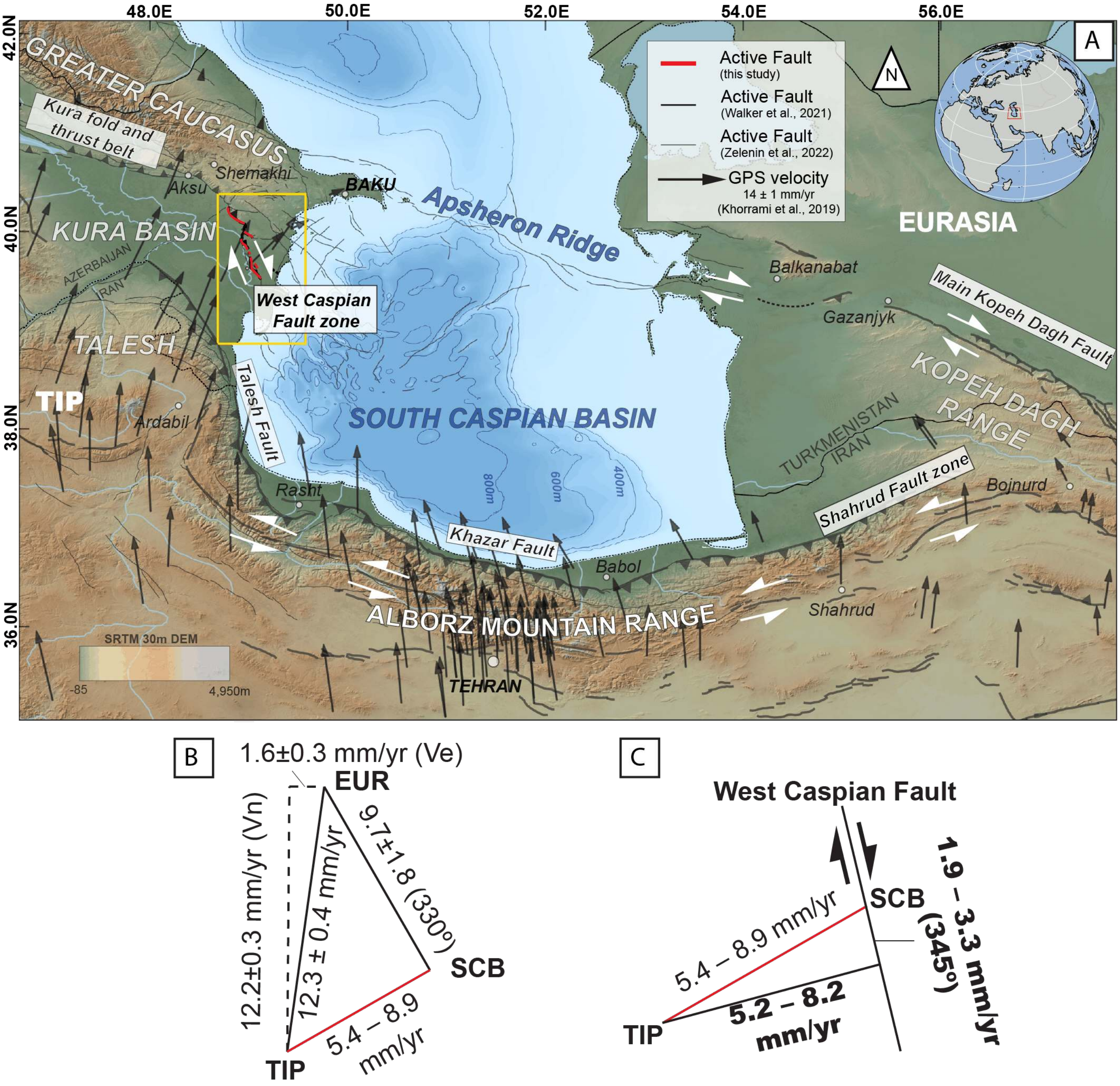

Figure 1 **A:** Tectonic map of the South Caspian Basin. Black arrows show GNSS velocity relative to Eurasia after Khorrami et al. (2019). Thick red lines are faults mapped in this study, thick dark grey lines are from Walker et al. (2021), and thin light grey lines are taken from Zelenin et al. (2022). Lines with teeth indicate thrusting. The map shows the northern zone of Arabian-Eurasian collision with the main fault zones named in the white boxes. The yellow box is the study area. Note that GNSS velocity vectors drop significantly north of the Greater Caucasus. The motion of the GNSS and on the faults shows the westward extrusions of the South Caspian Basin and the subduction beneath the Alborz and Talesh. **B:** Velocity triangle showing motion of the South Caspian Basin relative to Eurasia (Dodds et al., 2022). The Turkish-Iranian Plateau (TIP) motion is determined by averaging GNSS velocity vectors from Khorrami et al. (2019) relative to Eurasia. The dashed lines show the relative north (Vn) and east (Ve) velocities used to determine the TIP-EUR velocity vector. Solving between these two vectors gives SCB-TIP motion of 5.4 – 8.9 mm/yr. **C:** Projects the SCB-TIP motion onto the average strike of the West Caspian Fault (345°). This estimates the rate of shortening (5.2 – 8.2 mm/yr) and right-lateral shear (1.9 – 3.3 mm/yr).

eastwards directional change and decreasing magnitude of the velocity vectors between Salyan and Baku (Fig. 1, 2, and S1). Kinematic modelling from GNSS data show that N-S strike-slip is possible (Djamour et al., 2010; Kadirov et al., 2012). By forming a velocity triangle from GNSS-derived Talesh-Eurasia velocity and the 9.7 ± 1.8 mm/yr SCB-EUR velocity (Dodds et al., 2022), we estimate ~7.5 mm/yr of motion between the SCB and the Turkish-Iranian Plateau (TIP) and Kura basin (Fig. 1). Resolving this velocity onto the north-south structures of the TIP estimates 1.9 mm/yr of right-lateral motion, and 7.2 mm/yr of range-perpendicular shortening. Some of this shortening should be accommodated by reverse faulting uplifting the Talesh with the remain-

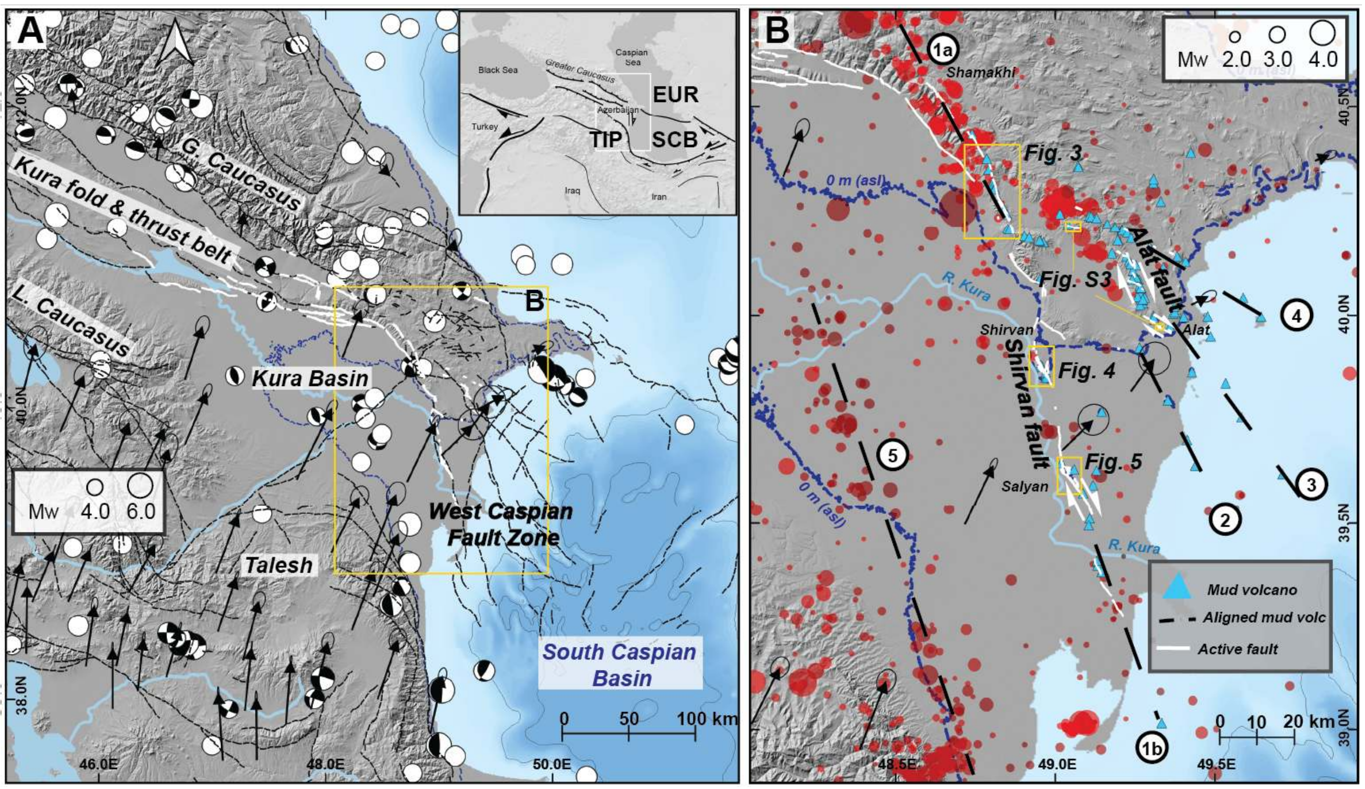

Figure 2 **A:** Seismotectonic map of Azerbaijan and Trans-Caspian region (inset). GNSS velocity vectors are from Khorrami et al. (2019), relocated seismicity is from Gunnels et al. (2020), and focal mechanisms are taken from the ISC catalogue (International Seismological Centre, 2026). Black lines are active faults from Zelenin et al. (2022). Digital elevation data is from SRTM (30 m resolution) NASA SRTM (2013) and bathymetric data is from the Global Oceans (https://www.gebco.net/data_and_products/gridded_bathymetry_data/). **B:** Dotted black lines show lineations of mud volcanoes in five main areas (1a – Shamakhi to Shirvan, 1b – Salyan to offshore South Caspian Basin, 2 – offshore southwest Alat, 3 – Alat (NW-SE) trend, 4 – north Alat offshore). Trend 5 is a linear NNW-SSE trend in seismicity.

der across the West Caspian fault zone.

The structures that accommodate relative motion between the Talesh and Kura basin are not well constrained, leaving questions regarding the kinematics of faulting. A number of north-south right-lateral earthquakes are known from the Talesh region of Iran, including the Mw 6.1 Ardebil earthquake in 1997, and right-lateral geological and geomorphic displacements are mapped on north-south faults within the Talesh (Aziz Zanjani et al., 2013). Gunnels et al. (2020) show a NNW-SSE striking linear trend of seismicity (greater than 30 km deep) in the Kura Basin (Fig. 2b – trend 5) and interpret this as a dextral strike-slip fault zone, the West Caspian Fault. An abrupt alteration in sedimentary thickness (Allen et al., 2002) and gravity anomalies (Khain et al., 1966) are thought to be indicative of the presence of the West Caspian Fault. Trifonov et al. (1986), Allen et al. (2002), and Khain et al. (1966) describe right-lateral shear and map active faults between topographic highs near Shirvan and Salyan, documenting evidence for en echelon folding.

2.3 Caspian Sea level

The Caspian Sea is the largest landlocked body of water globally, with occasional outflow to Black Sea during some interglacial periods (Leroy et al., 2020). The closed nature of the Caspian Sea means that water levels vary depending on climatic and river inflow changes. The main sources of water into the Caspian are the Volga, Kura, and Amu-Darya rivers and occasionally the Aral Sea.

The Caspian sea level is presently at -28 m a.s.l. and has changed dramatically since the Miocene, with transgressions peaking above 150 m and regressions as low as -1500 m (Forte and Cowgill, 2013; Kroonenberg et al., 1997). Radiocarbon dating of marine shells around the Caspian indicates two significant late Pleistocene transgressions at around 35 ka and 11–13.5 ka with highstands of 48–50 m and 0 m above global mean sea level (a.s.l.), respectively (Arslanov et al., 2016; Dolukhanov et al., 2010; Kakroodi et al., 2012; Kroonenberg et al., 1997; Pánek et al., 2016). During the Holocene, the Caspian Sea level has fluctuated with frequent transgressions and regressions, and with a maximum highstand of -20 m a.s.l. (Kakroodi et al., 2012; Kroonenberg et al., 2007; Ollivier et al., 2016).

3 Methods

3.1 Satellite imagery

We obtained high-resolution stereo imagery from the Pléiades satellite mission to build digital elevation models (DEMs) of onshore topography around the Shirvan fault zone (https://portal.opentopography.org/

dataCatalog, 19/05/2021, SO21034807-2). We use Agisoft Metashape software to match points from pairs of images and calculate elevation point data. The point data is then interpolated to build a surface model or DEM with 1 m/pixel resolution. Faults were remotely mapped using hillshade images of these Pléiades DEMs, Google Earth, and Bing Aerial images prior to field mapping in May 2022. Using the satellite images and derived DEMs, we identified key sites for further field investigation. The Pléiades-derived elevation data is geoid-adjusted using the emg2008-5 model derived by satellite gravity data and cubic interpolation (Karney, 2019). We use the geoid-adjusted elevation data to determine relative topographic heights.

3.2 Structure from motion (Surveys using Uncrewed Aerial Vehicle)

Key study sites near Salyan (Fig. 2b) were surveyed using a Teokit-equipped DJI Phantom 4 Pro v2 drone, collecting ground surface images. The Teokit is a dGPS and provides precise photo locations that are corrected to the Emlid Reach RS2 dGPS base station (e.g., Zhang et al., 2019). We use Agisoft Metashape software to process the surveyed photographs into an orthomosaic, and a DEM with a horizontal 2.6 cm/pixel resolution (https://portal.opentopography.org/dataCatalog).

3.3 Geomorphic and fault mapping

We produced geomorphic maps using a combination of field observations, satellite imagery, and drone-derived DEMs. At the Salyan site, we identified fault scarps and measured deflected drainage channels using the drone imagery.

We used abandoned terrace risers as piercing lines to measure deflections at the Salyan site as the thalweg is still the active channel at the site. Deflections were measured in QGIS using the distance between the thalwegs and risers (e.g., Kurtz et al., 2018), in the field and using the LaDiCaoz (version 2) tool (e.g., Haddon et al., 2016; Zielke and Arrowsmith, 2012). The tool uses a best-fit method to restore drainage channels and terrace riser slope. We use this tool with elevation data from our UAV derived DEM, and our fault and geomorphic mapping to determine the amount of drainage deflection.

3.4 Paleoseismic Trenching

At the Salyan site, two paleoseismic trenches were excavated, cleaned, gridded, photographed, and logged. As a base for the trench logging, we used an orthophoto mosaic constructed using photographs captured with a Samsung Galaxy S20 Ultra and processed in Agisoft Metashape software. The orthophoto has been scaled and oriented using reference points extracted from iPad-lidar scans of the trench walls (Pierce and Koehler, 2023). Logging was performed on an iPad using Adobe Illustrator software. Units, faults, and folds were distinguished, divided, and described following paleoseismic methods described in (McCaplin, 2009). Using the Emlid Reach RS2 dGPS base station and rover, we measured an elevation profile along each trench. In addition, a sediment sample pit 2.3 m deep was excavated into a terrace at the Salyan site, to obtain datable sediment to establish constraints on geologic slip.

3.5 Quaternary dating

Samples were collected for both radiocarbon and infrared stimulated luminescence (IRSL) dating (Table S1). Charcoal nodules in a burn layer were found in very fine aeolian sands at 2.1 m depth in the sample pit and sampled for radiocarbon dating. We also sampled two intact marine bivalve shells in Trench 1. Charcoal nodules and marine shells were analysed at Beta Analytic laboratory in Miami, Florida. Results were calibrated using OxCal v4.4 (Bronk Ramsey, 1995) with the Marine 20 calibration curve and DR adjustment (-128) for the Caspian Sea shown in Table S2.

For IRSL dating we analysed 10 sediment samples from Trench 1 and 3 samples from Trench 2. Sample tubes were hammered into the sediment layer and sealed from light contamination. The ends of the tubes were wrapped in aluminium foil and taped to seal. The samples were processed in the Luminescence Dating Laboratory at the University of Sheffield and analysed using IRSL dating techniques on single feldspar grains (Rhodes, 2015). The IRSL dating results are provided in full in Table S1 and are detailed on the trench logs. We apply the finite mixture model to identify grouping within the equivalent dose distributions (Galbraith and Green, 1990).

4 Right-lateral strike-slip faulting in the Kura basin

The West Caspian Fault zone comprises a system of faults, notably the Shirvan and Alat faults that have a clear surface expression. Other faults in the West Caspian fault zone are inferred by lineation and concentration of mud volcanism and seismicity (Fig. 2 and S1).

4.1 The Shirvan fault

From satellite imagery and field observation we identify a zone of right-lateral strike-slip faults at the eastern margins of the Kura basin. We describe three sections where faulting is clearly visible in geomorphic surfaces. Each of these sections is associated with larger-scale topography caused by fault bends and mud volcanism. Mud volcanoes are aligned along the fault trace, with concentrations near bends in the fault, corresponding to pressure ridges. We note that the alignment in mud volcano activity extends south of the observable end of the fault zone, providing further evidence that the fault is longer than visible in the geomorphology. We infer that the fault zone extends between the three parts described here, but with a subtle geomorphic expression within the low-lying parts of the Kura basin. Seismicity follows an ~150km-long NNW-SSE alignment, with depths of 40 km, which extends from Shamakhi through Shirvan and Salyan, and ~100 km offshore into the Caspian Sea (Fig. 2).

In Fig. 3 we show east-facing scarps running along the apex of topography and an alignment of mud volcanoes south of Shamakhi. We identified lateral displacements across this section of the fault and we infer that a major component of the slip is right-lateral, based on the scarp morphology, deflected drainages, and aligned valleys and hills.

Linear scarps cutting across higher topography adjacent to Shirvan are shown in Fig. 4. The scarps are both uphill and downhill facing (shown in profiles in Fig. 4a & d). We find several right-laterally offset drainages. There are too few identifiable offsets in our dataset to give a robust statistical analysis. However, we find right-lateral deflections between 5 and 20 m for a series of continuous creeks.

There are stepovers along the fault trace that are both left and right stepping (Fig. 4b and c). At the left step we see a topographic high bounded on each side by a rupture strand (Fig. 4b), indicative of right-lateral motion. We also see a depression within a right step in the surface rupture trace in this zone (Fig. 4c), consistent with transtension and right-lateral faulting.

Near Salyan we identify a linear fault trace bounding the western side of a flat-topped region of raised topography, in which steeply dipping strata crop out and have been eroded during a highstand (Fig. 5). Shelly marine terrace deposits are preserved on the surface in places.

The fault trace along the western side of the fold bends from almost N-S in the north (Fig. 6) to NW-SE in the south (Fig. 5). Small antithetic left-lateral faults displace vertically dipping beds (Fig. S2f).

We visited a section of the fault in the field, where the main fault trace runs along an ~8 m-high scarp along the base of a marine terrace. At this site we used an UAV to produce a DEM, excavated two paleoseismic trenches through the fault zone, and opened a soil pit in an adjacent terrace surface. From the UAV-derived DEMs and field mapping we measured offset terrace risers displaced right-laterally by 8 m and 54 m across the main fault trace (Fig S2).

The Shirvan fault bend at Salyan (Fig. 5) also shows other antithetic structures away from the main fault trace. We observe antithetic left-lateral faulting trending N-S shown by fractures and offset bedding planes in vertically dipping bedrock (Fig. 5 and S2f). The N-S orientation of these left-lateral structures is antithetic to the trend of the Shirvan fault at this bend. There is no expression of these faults in the recent geomorphic surfaces, leading us to speculate that these do not extend far and are secondary to the main Shirvan fault.

4.2 The Alat fault system

To the west and northwest of Alat there are scarps with right-laterally offset drainage channels, trending NW-SE to WNW-ESE along the western margins of a range of folds and mud volcanoes (Fig. S3). The right-lateral displacements are particularly clear in the region shown in Fig. S3, where a sharp linear fault trace tracks across the slopes of a large mud volcano crosscutting topography. A series of small channels and their interfluves are consistently displaced by ~10 m.

Further south, right-lateral offsets are again visible where the fault scarp cuts across mud flows (Fig. S3(e)). In this example the lateral offsets are less well defined, though larger, than in Fig. S3(b). Incised channels show displacements of several tens of metres.

The Alat fault system as mapped from the geomorphology coincides with an alignment in mud volcano activity, which extends offshore and splits into three separate trends, numbered 2, 3, and 4 in Fig. 2. There is also a close correlation between the mapped fault and an alignment in shallow seismicity, with depths to ~20 km (Fig. 2), and appears to merge with the Shirvan fault zone seismicity near Shamakhi (Fig. 2).

4.3 Faulting inferred from mud volcanism and seismicity

We have described the Shirvan and Alat fault systems (alignments 1–4 on Fig. 2). These are expressed in the geomorphology, alignment of mud volcanoes, and relocated seismicity in the Kura Basin by Gunnels et al. (2020). We use these alignments to infer that the Shirvan and Alat faults are longer than geomorphically expressed at the surface and extend offshore into the Caspian Sea (Fig. 2 and 3).

We observe another alignment of seismicity with an NNW-SSE trend parallel to those we have already described, but sited further west in the interior of the Kura basin (Fig. 2, alignment 5). Regional seismicity observed in Gunnels et al. (2020) and the ISC/GEM seismic catalogue also show strike-slip focal mechanisms along this trend. The seismicity is mostly deep along this trend (>20 km). However, we do not observe a surface expression of faulting or mud volcanism in this region.

5 Paleoseismology of the West Caspian Fault

5.1 Geomorphology at the Salyan trench site

At the Salyan site, a small stream cuts through the marine terrace/platform. Incision of this stream, possibly due to a combination of faulting and decreasing marine base level, has left behind a suite of terraces. These terraces and the margin of the marine platform are cut by a clear NW-striking fault.

We interpret fluvial, alluvial, aeolian, and marine deposits demonstrating changes in depositional environment. Qt1 is the youngest fluvial terrace bound by the active channel and an older terrace riser (Fig. 6). The grain size ranges from silt to medium sand with scattered pebbles. The vegetation is mainly scrub bushes forming in mounds up to 0.5 m wide, and we observe a change in the concentration of vegetation at a small 0.2 m NNW-SSE scarp across the terrace (~25 m in length).

Qt2 is separated from Qt1 by a 0.5m-high terrace riser and consists of brown silt with grass and small scrub bushes. The surface has a slight slope towards the active channel, and it has a smooth surface with little incision.

Qt3 sits at a higher elevation than Qt2 and is separated from Qt1 by a terrace riser. Qt3 sits only on the

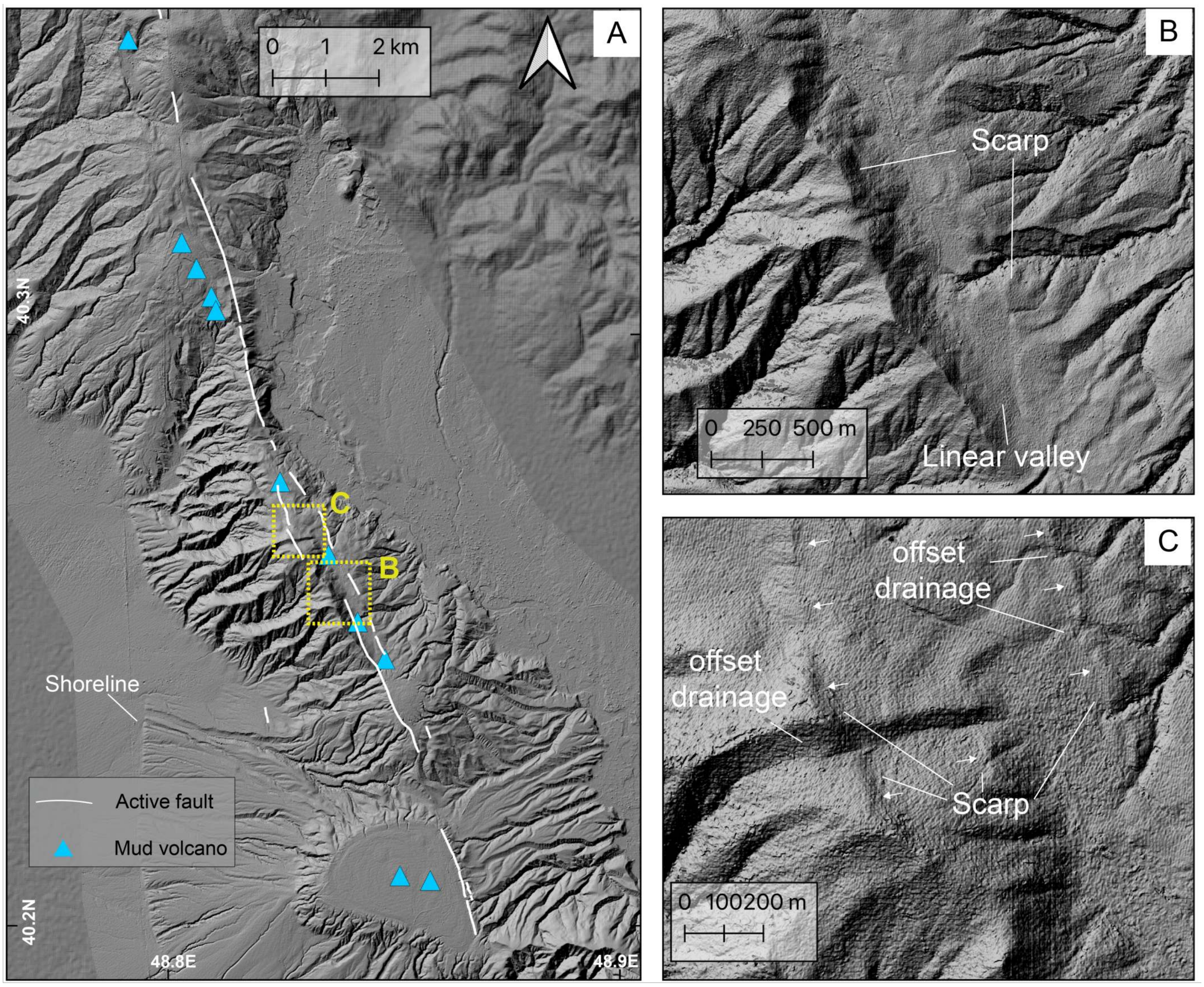

Figure 3 NNW-SSE striking strike-slip faulting between Shirvan and Shamakhi (Fig. 2). **A:** Active faulting on Pléiades 1m DEM. Mud volcanoes form in a lineation along fault strike. **B:** A scarp forming along a linear valley. **C:** Multiple scarps with offset drainages (right-lateral). White arrows indicate the fault trace.

NE side of the fault trace and higher in the channel than Qt1 and Qt2. The surface consists of a brown silty soil with sparse grass and scrub bush vegetation and has a slight incline of 10° towards the north-west. The surface is bound by a 10 m terrace riser and a 1 m fault scarp to the south-west.

Qt4 is a flat 10 x 10 m terrace deposit higher in the drainage channel and only found on the NE side of the fault trace. Qt4 sits at a 5 m higher elevation than Qt3 and is bound to the SE by a 5 m riser. There is sparse vegetation of grass and small scrub bushes and the terrace sediment is composed of light brown silt.

Qaf is a fan-shaped deposit that extends into a gully. The surface sits topographically above the Qt1 surface adjacent to the Qad surface. There is no riser between Qaf and Qad. A riser exists between Qt1 and Qaf deposits and suggests that Qt1 was incised into Qaf. The Qaf surface drains to the south-west and we observe that it traces back to the foot of the Qmt riser where there is a small gully. The majority of the Qaf surface is offset from this incision to the NW along the fault scarp.

Qad is a bumpy, sparsely vegetated surface consisting of light brown to straw yellow silty sediments. Abundant marine shells are observed on its surface. From the elevation data we observe that this deposit ramps against the fault scarp to the east and the surface has a slight incline. A sample pit was excavated into this surface at the northwestern part of Fig. 6, in which we observe silts to very fine sands, with layers of pebbles. We also found a layer rich in charcoal nodules within aeolian deposits capping a marine sand layer, that we interpret as a burn layer. We sampled and analysed these charcoals from a depth of 1.4 m, and these yield an age of 1744–2145 yrs cal BP. We also sampled and dated one of the marine shells on top the terrace surface, yielding an age of 35,280 ± 240 years cal BP. We interpret this as scattered shells on the surface, reworked from numerous marine and shelly deposits seen in the in-situ marine terrace above.

At the highest elevation in our study area (approximately 0 m a.s.l.) is a flat terrace, mapped as Qmt (Fig. 6). There are several small (~1 m wide) shallow

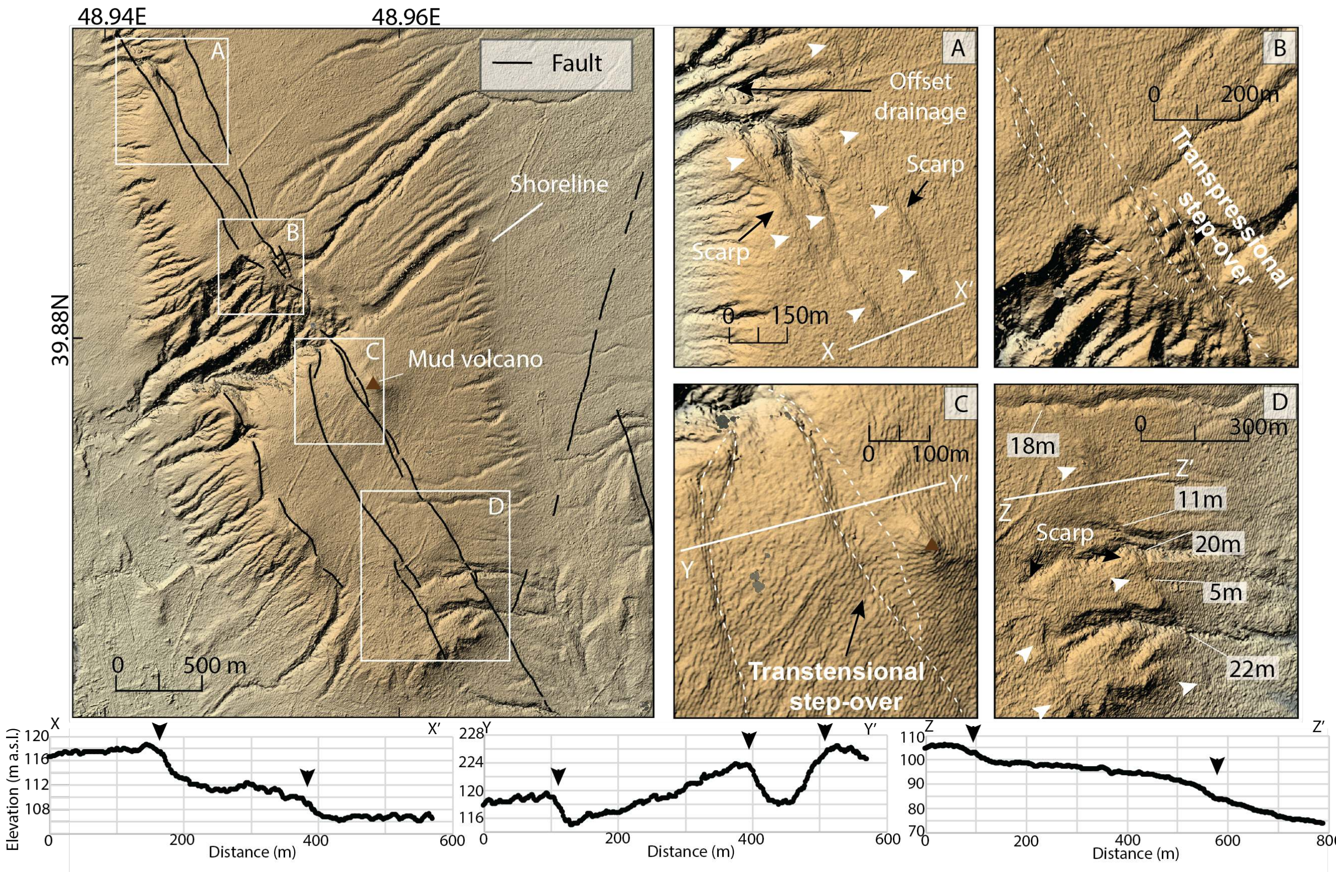

Figure 4 Fault map near Shirvan shown on a DEM derived from the Pléiades satellite imagery (1 m resolution). **A:** The rupture trace in three strands that have created scarps in the topography. The topographic profile XX' shows the scarps. There is also an offset drainage along strike of the rupture trace at the NW of the panel. **B:** The rupture trace and a transpressional step-over (pop-up) structure. **C:** Rupture trace showing scarps and trantensional pull-apart basin within a step-over. This is seen in the topographic profile YY'. **D:** Two rupture traces, scarp, and offset drainage channels with measurements between 5m and 22m. Scarps can be seen in the topographic profile ZZ'.

pits previously excavated into this surface up to 30 cm deep and we observe brown silty sands containing broken marine shells in the surface. We interpret this surface as a marine terrace. We did not sample in-situ shells from the Qmt surface to confirm its age. The surface elevation of 0 m a.s.l. is consistent with formation during the 11–13.5 ka transgression. We interpret Qmt as the oldest geomorphic surface in the Salyan study area. Also, as the most recent Caspian transgression at 11–13.5 ka would have inundated the Salyan trench site, we assume that the landscape was reset at that time, with all terrace formation and incision (Qt1–4) being younger than the highstand.

5.2 Trench 1

Trench 1 (Fig. 6) is 18 m long and 3 m deep from the top of scarp to the bottom of the excavation. The topography is raised forming a 0.5-m-high scarp across the width of the Qaf surface (~6 m). The trench was excavated across this 0.5 m scarp, into the Qaf and Qt3 deposits. An orthophoto mosaic and log of the northeast wall is shown in Fig. 7. The trench exposes a sequence of sedimentary deposits that are cut by two distinct zones of vertical and sub-vertical fractures either side of the scarp. At these fracture zones we observe sharp contacts and changes in the sedimentary deposits.

5.2.1 Stratigraphy

We group sedimentary units exposed in trench 1 into four groups. At the base of the trench, the oldest group (Group 1) consists of two units; chocolate brown clays (U10) and blue bedded sands (U20). The bedding planes are delineated by lighter blue and darker blue/black bands of fine to medium grained sand. We interpret Group 1 as low energy lakebed sediments.

Group 2 (U50, U60 and U65) is found between the two fracture zones and sits above Group 1. Group 2 contains intact marine shells, small well-sorted pebbles and coarse to fine well-sorted sands (Fig. 7). U50 is a fine to medium grained cross-bedded deposit that is capped by a ripple-laminated sand unit (U60). We observe salt layers within units U60 and U65, leaching from the trench wall. From the sedimentary structures and presence of shelly material we interpret the sands as a near-shore or beach deposit.

Group 3 consists of units U30, U40, U45, U80, U100, and U130. Grain size ranges from fine sands to silts. U30 is a bedded fine sand and silt deposit that extends

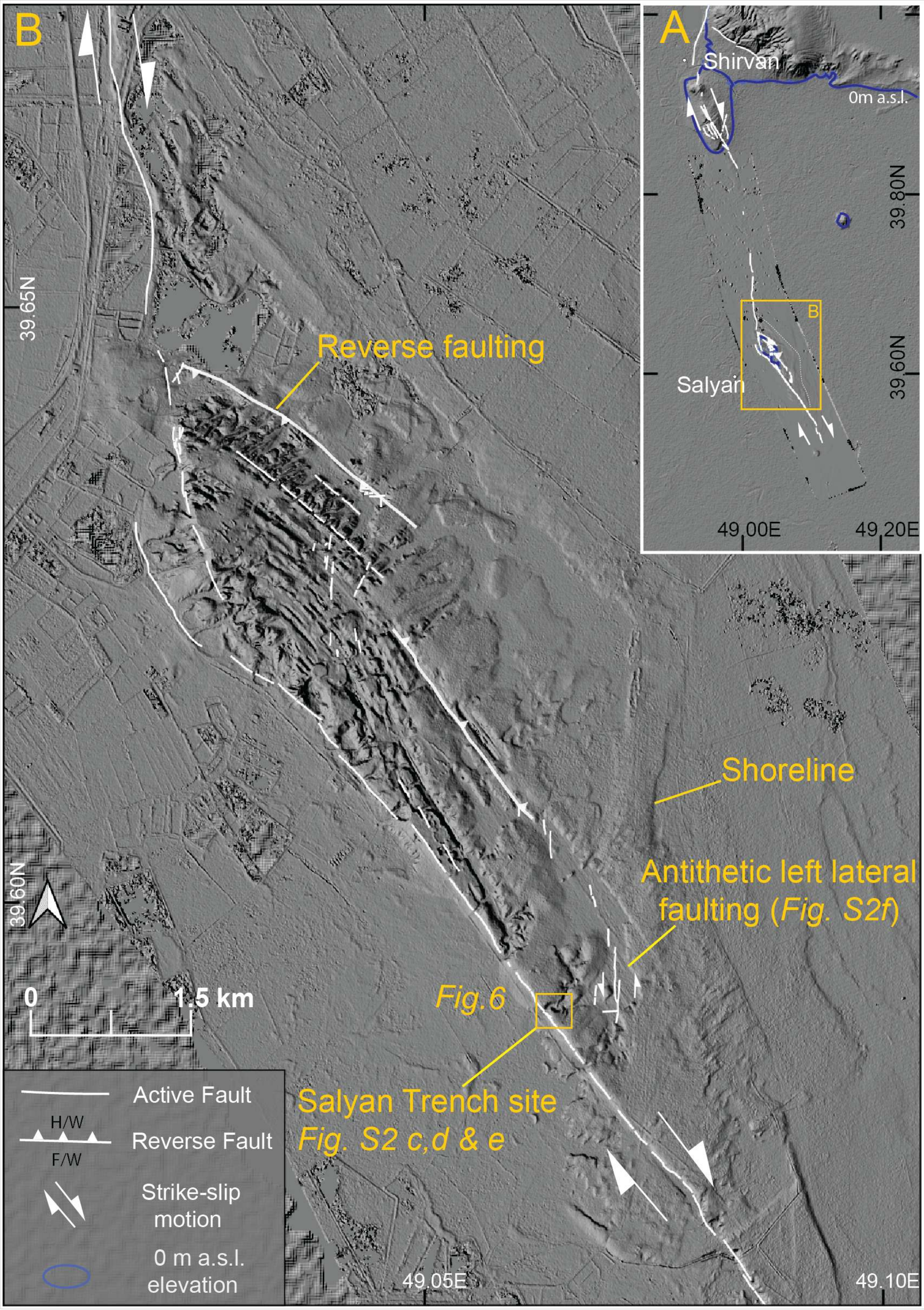

Figure 5 **A:** Pleiades-derived DEM of the Salyan region of the Shirvan fault. White lines delineate active faulting from our field and remote mapping. **B:** Study area from A. The fault bends from a N-S to NW-SE trend. We identify antithetic R' sinistral faulting (Fig. S2f). Trench site is shown in the yellow box on panel B. Blue lines on inset panel show 0 m a.s.l.

across the F2 fracture zone forming an erosional unconformity with the lower units. It has an undulating contact and channel structure cutting into the blue sand (U20). Southwest of F2, U30 forms a sharp angular un-

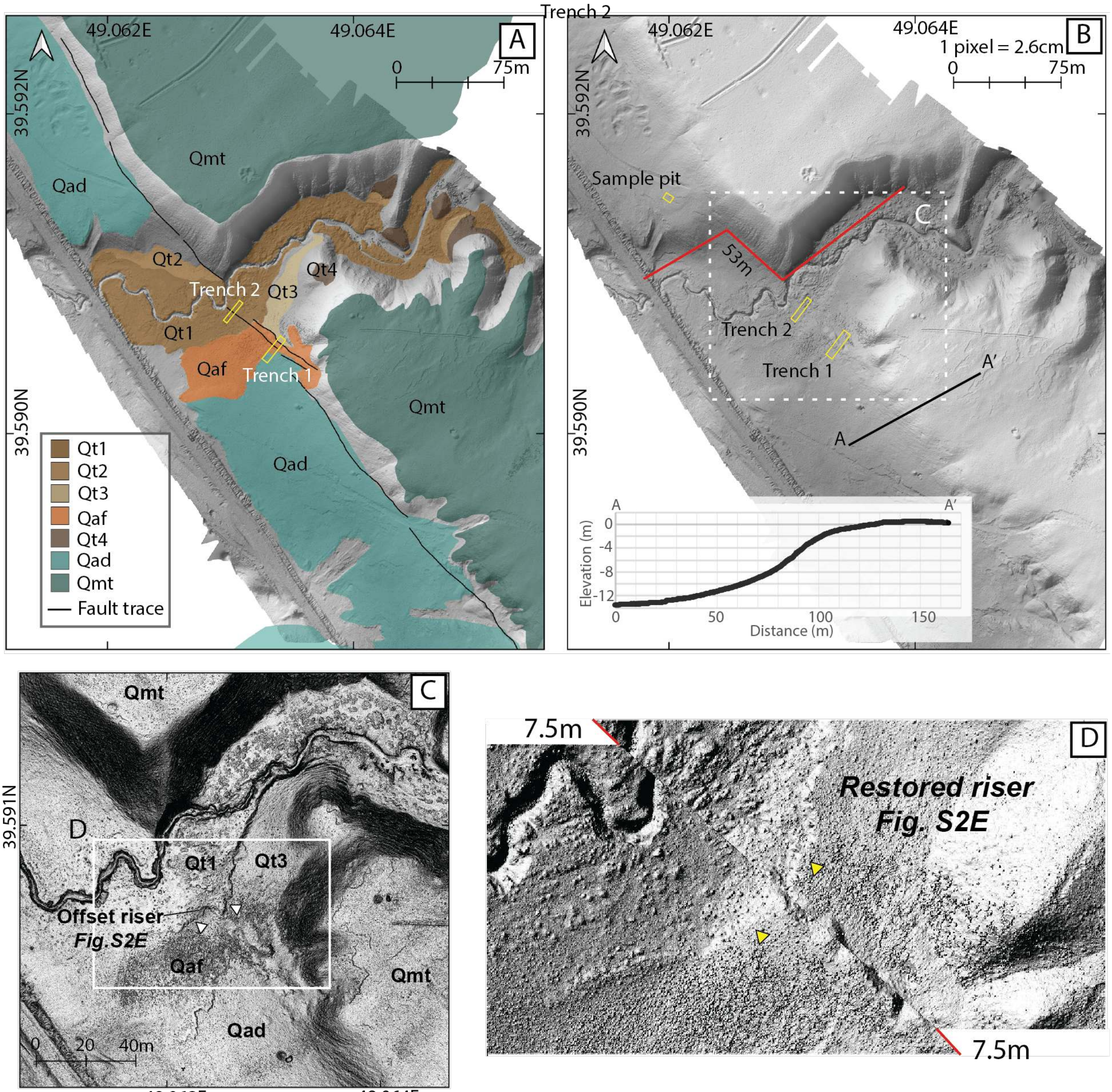

Figure 6 UAV-derived DEM of the trench site near Salyan on the Shirvan fault zone. Panel **A** shows a geomorphic map and the fault trace. Panel **B** is a hillshade of the UAV DEM showing the sample site, Trench 1 and Trench 2, and a riser right-laterally offset by 53 m. Profile AA' shows the marine terrace at an elevation of 0 m a.s.l. Panel **C** shows a slope map of from the UAV DEM data, showing the offset Qt1 riser and Qt1 tread. The matched riser profiles are restored using LaDiCaoz method, and the result is shown in panel **D** showing a 7.5 m offset.

conformity against U65 below. Above U30, northeast of F2, there is a finer grained bedded silt unit (U40), this layer is laterally truncated at a fracture zone. This unit is capped by a bedded block silt layer (U45) that also truncates at the fracture zone. Above U45 there is a blocky silt unit (U130) that almost caps the entire trench. Above U30 southwest of F2, there is a distinct unit (U80) that has interstitial beds of fine sands and laminated silts; this unit abuts U40 and U45 across F2. U80 sits above U30, northeast of F1 and is a unit of laminated fine sands and silts. U100 sits above U80 and is a laminated silt layer with a varying thickness across the trench. It is a distinct laminated silt layer, without fine sand. Both U80 and U100 have bed thicknesses changes at fault F1. We interpret these units as overbank or flood plain deposits, with thickness variations being juxtaposed because of lateral fault displacements. We interpret Group 3 as fluvial/alluvial in origin, with sediment washing down from the marine terrace (Qmt) above.

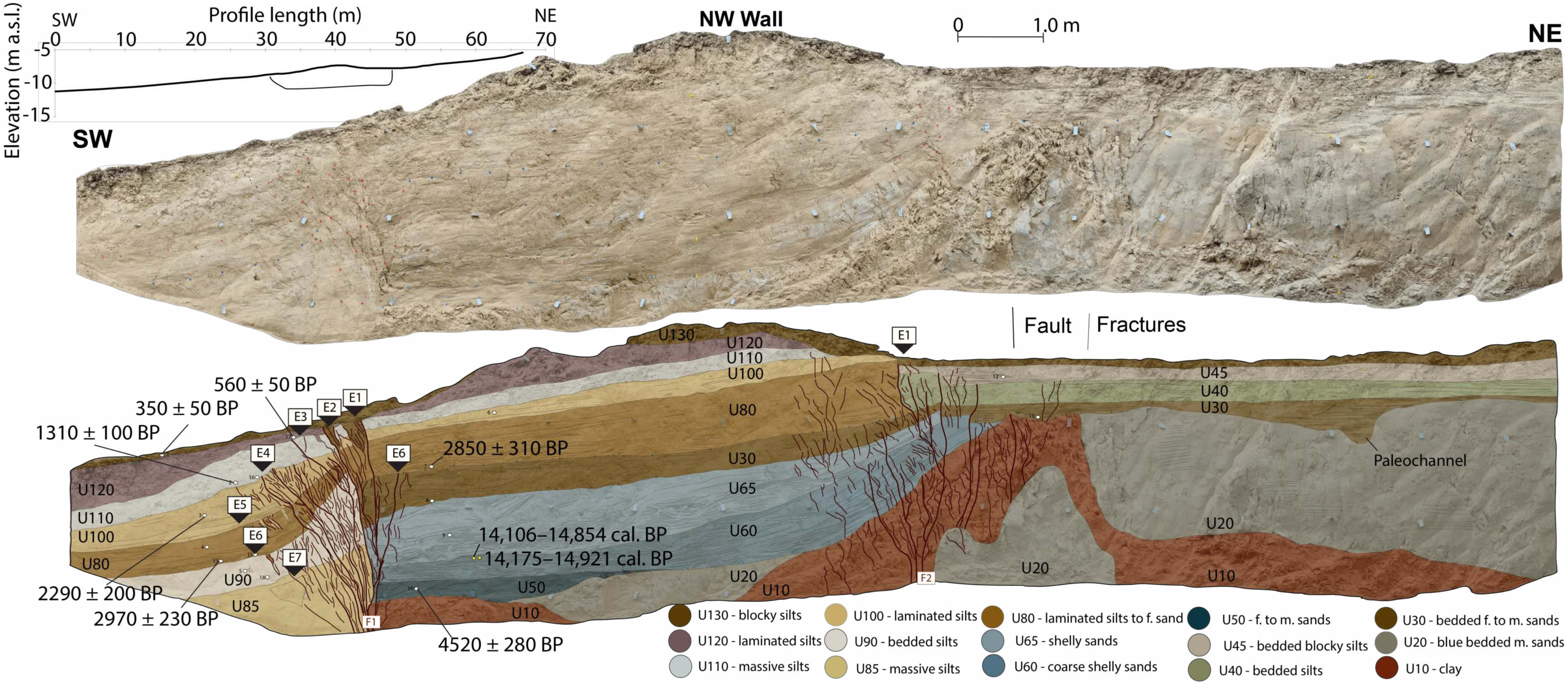

Figure 7 Trench 1 – photo-orthomosaic and trench log of the NNW wall of Trench 1 (Fig. 6). The trench has two fault zones (F1 and F2) and seven possible events (E1–7). A topographic profile was measured along the extent of the trench wall and extended at either side using a dGPS.

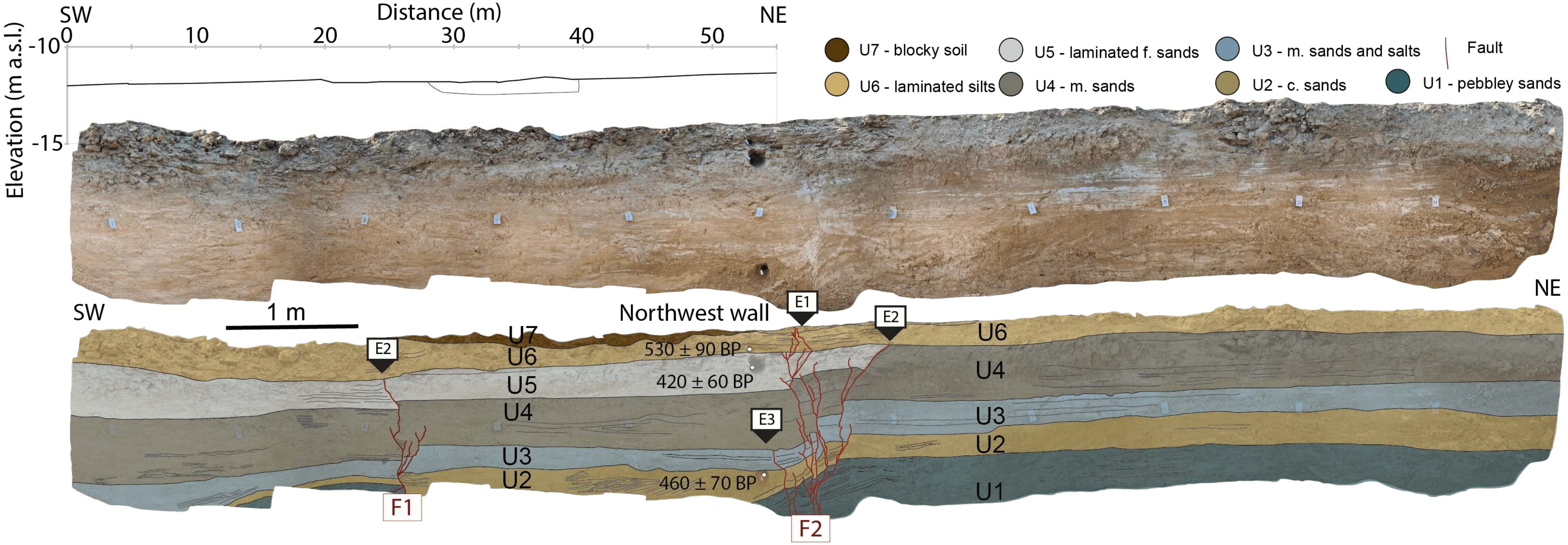

Figure 8 Trench 2 – photo-orthomosaic of the NNW wall of Trench 2. Trench log shows fluvial sediments in the Qt1 surface (Fig .6). There are two fault zones (F1 and F2) and up to three events (E1–3). A topographic profile, measured using a dGPS, showing the trench location is shown in the top left corner.

Group 4 consists of entirely of silts with differing sedimentary structures (U85, U90, U110 and U120). At the base of the trench at the southwestern end there is a thick unit of massive silts with no discernible bedding or lamination (U85). Above this unit there is a bedded silt unit (U90) with a variable thickness at the southwestern facture zone. Units U80 and U100 overlie U90 southwest of F1, thinning in the fracture zone, and interrupting the sequence of massive silt units. U110 sits above U100 and is a thin deposit of massive silts with no lamination or apparent bedding. Above U110 there is a blocky silt deposit, U120, that shows some lamination. We interpret Group 4 as a package of wind-blown dust deposited against a scarp.

5.2.2 Faulting and related deformation

The sediment deposits are deformed at two distinct vertical boundaries in a series of fanning fractures forming a flower morphology. The fractures terminate at different levels throughout the sedimentary sequence. We observe vertical offsets and bedding thickness changes in the sedimentary layers (U80, U100, and U110) across these fractures at the southwestern end of the trench. The lower units (U60 and U65) have variable dip from almost horizontal at the southwestern end to 30°W towards the northeast. There is an angular unconformity between the marine sediments (U60/65) and the overlying laminated silts and sands (U30).

The lateral truncation of sediments, across-fracture bed thickness changes, vertical offsets in sediment layers, and the flower structure are diagnostic of strike-slip faulting. We interpret that the clay (U10), blue sand (U20), and the shelly sands (U50, U60, and U65) are folded. The sedimentary structures within Group 2 do not show evidence of onlap and do not appear to be high angle slope deposits so were most like deposited horizontally or on a slight incline.

5.3 Trench 2

We excavated an 11 m-long and 1.5 m-deep trench across a subtle ~0.2 m high scarp in the Qt1 terrace (Fig. 6). An orthophoto mosaic and trench log of the northwestern trench wall are shown in Fig. 8.

5.3.1 Stratigraphy

In Trench 2 there is one sedimentary facies of fluvial sediments consisting of seven units. The units fine upwards and all show sedimentary structures ranging from channel cross stratification to lamination in the upper units. Unit 1 (U1) consists of medium to coarse sands containing pebble layers; above this sits a coarse sand layer (U2) and then a layered medium sand deposit containing salts (U3). This is then topped by a relatively thick medium sand layer (U4). On the downthrown side of the fault U4 is capped by a laminated fine sand layer (U5). We cannot trace this layer on the northeastern side of the fault. The length of the trench is then capped by laminated silts (U6) and a blocky silt deposit (U7).

5.3.2 Faulting

We observe two zones of vertical fractures offsetting and truncating sedimentary units. The first zone is 3 to 4 m from the southwestern end of the trench. The fractures do not extend to the surface. The second zone occurs beneath the subtle scarp at 6 to 7 m from the southwestern end. The fractures extend to the surface and are vertically corrugated, with splays terminating in the lower units. We interpret these two fracture zones as faults. Both faults rupture layers U1 to U5 and with the F2 fault also rupturing to the modern ground surface in terrace Qt1. Units U4 and U6 cap fault ruptures suggesting two earlier earthquakes. Overall, we interpret three events from the two fault zones.

5.4 Geochronology

Our age control comes predominantly from single grain infra-red stimulated luminescence (IRSL) dating of feldspar grains, due to the absence of suitable organic remains for radiocarbon dating in most of the stratigraphic layers. The detailed results of the 13 IRSL samples we processed and analysed are shown in Table S1 (calendar age before 1950). The results from Trench 1 show a consistent stratigraphic order increasing in age with depth from 350 ± 50 to 4520 ± 280 BP years (Fig. 7). At the southwestern side of fault F1 in Trench 1, sediment age increases by ~1000 years per 0.5 m of depth. Across F1 we see good agreement in age between the base of U80, with ages 2970 ± 230 and 2850 ± 310 BP years, supporting our interpretation that these layers are part of the same deposit.

Near the bottom of Trench 1 we sampled a fine to medium tabular cross-bedded deposit (U50) yielding an age of 4520 ± 280 BP years. Above this sample two intact marine shells were extracted from U65 and dated using radiocarbon (Table S2), yielding ages of 14175 –14921 and 14106–14854 cal. BP at an elevation of -13.8 m (a.s.l.). The sedimentary structures within Group 2 are interpreted as shallow marine or shoreface environment, and the elevation is consistent with the high stand at 11,000–13,500 years ago, but the IRSL age suggests instead that the deposit is younger (4520 ± 280 BP years) and postdates all major Caspian transgressions. In the following sections we base our interpretations on the assumption that the IRSL ages are correct, and that the Group 2 units represent reworked marine debris.

In Trench 2 the IRSL ages are inverted with U6 dated at 530 ± 90 BP years, U5 420 ± 60 BP years, and U2 at 460 ± 70 BP years, albeit within error. The age results of layers U2 and U5 are in stratigraphic order with the upper younger layer U6 measured at a slightly older age. All the samples are taken from Qt1 fluvial terrace and are within the error of each other. We therefore conclude that this terrace was formed by a series of sediment pulses most likely occurring between 360–620 BP years.

5.5 Paleo-earthquake history

To constrain the timing of paleoearthquakes, we developed a Bayesian chronological model using OxCal based exclusively on IRSL ages from Trench 1. This approach was adopted because stratigraphic correlations and event horizons between Trenches 1 and 2 are not sufficiently robust to justify a combined model. Although several units and event indicators appear similar across both trenches, lateral variability and exposure limitations introduce uncertainty in their equivalence. We therefore chose a conservative strategy that avoids propagating potential miscorrelations into the age model. Nevertheless, the three youngest events identified in both trenches are interpreted as likely correlative based on their stratigraphic position and overlapping age constraints. This correlation is considered reasonable but cannot be demonstrated unequivocally, and we acknowledge the possibility of missing or misidentified events in either trench.

Event 1 In Trench 1 fractures propagate through all the sedimentary units and terminate in the uppermost deposit (U130) at both faults (F1 and F2 in Fig. 7). We observe that sediment fill in buried fissures beneath U130 has a sheared fabric at the top of fault F1 (Fig. 9). In Trench 2 fractures also reach the present-day surface at the top of fault F2 but note that fault F1 does not appear to rupture the present-day surface. Based on the sediment deposits in Trench 1 we bracket this event must postdate U120, but its age relative to the dated sample within U130 is uncertain. From the single-grain IRSL results this event has most likely occurred after 560 ± 90 years. In Trench 2 we likewise have only a lower bound on the age of the MRE from the single-grain IRSL results of 530 ± 90 years BP (Fig. 9). We are unable to tie this event to the historical archive of seismic events > M6.

Event 2 The penultimate earthquake is marked by filled fissures in Trench 1 (Fig. 7 & 9) and capped fault terminations in Trench 2 (Fig. 8 & 9). The fissure fill material in Trench 1 is U130 and has been dated at 350 ± 50 years BP. Therefore, the event is bracketed between U130 and U120 which yields an age of 457 ± 76 BP years. In Trench 2 there are fracture terminations in the unit U5 at both the F1 and F2 faults. These fractures are clearly capped by the U6 laminated silt layer. We also observe small vertical offsets at the base of the U5 unit at both faults (Figs 8 & 9). U6 yields an age of 530 ± 90 BP years, which provides constraint on the timing of event 2 in this trench. It does not fully correlate with the age of Event 2 in Trench 2. Given the younger age of U5 (420 ± 60 BP years) beneath U6, and the proximity of Trench 2 to Trench 1, it is likely that this was the same event.

Event 3 We observe evidence for the third most recent event in both Trench 1 and 2. In Trench 1, we observe terminating fractures and a buried fissure at the top of unit U110 (Fig. 9). These fractures are capped by a laminated silt layer (U120) and the buried fissure is filled with similar material (colour and composition). The age of U120 is provided by IRSL sample SAL1-17 at 560 ± 50 years BP (Fig. 9, Table S1), and provides a minimum age of rupture. The bottom of U110 yields an age 1310 ± 100 BP years, providing a maximum age constraint. These constraints provide a probable age of event 3 of 941 ± 224 BP years (Fig. S4). Trench 2 shows faults terminating and capped bedding in layer U4 (Fig. 8 & 9), which also supports the hypothesis of an additional event. However, the age constraints from Trench 2 bracket this event between 420 ± 60 BP years (U5) and 460 ± 70 BP years (U2). This is much younger than the constraints provided in Trench 1.

Event 4 In Trench 1, we observe a series of faults and fractures terminating at the top of unit U100. These terminations are capped by a massive silt layer (U110) (Fig. 7 & 9). The capping layer (U110) was sampled and dated at 1310 ± 100 years BP, with the layer beneath (U100) dated at 2290 ± 200 years BP. Therefore, we have constraint on the timing of Event 4 between those two ages. From the termination of the fault rupture in the stratigraphy the event timing is closer to 1310 ± 100 years BP.

Event 5 We observe a set of three buried fissures and a cluster of sealed fractures terminating in unit U80. These features are capped by laminated silts (U100). The middle of U100 was sampled and yields an IRSL age of 2290 ± 200 years BP. We took two samples from the base of U80 at either side of F1 and these yield an IRSL ages of 2970 ± 230 and 2850 ± 310 BP years (Fig. 7 & 9). We conclude that this event probably occurred around 2547 ± 236 BP years.

Event 6 In Trench 1, on the southwest side of fault F1, the base of U80 caps a set of clustered fractures and a small fissure in a bedded silt layer U75. On the northeast side, ruptures break through U30 and are capped at the base of U80. We sampled the base of U80 on both sides of fault F1. IRSL samples on the northeast and southwest sides of fault F1 yield ages of 2850 ± 310 years BP and 2970 ± 230 years BP respectively. These results are within error, showing agreement on either side of the fault (Fig. 7 & 9). We have IRSL age constraint on unit U50 near the bottom of the trench on the western side of fault F1 of 4520 ± 280 years BP. Therefore, we can only provide a wide constraint on Event 6 of 4724–2964 BP years. However, if the radiocarbon ages of the shells in U65 accurately reflect the time of deposition, then Event 6 is poorly constrained between 2850 ± 310 years BP and 14548 ± 373 years cal. BP. Since the samples constraining the upper age are taken near the base of the rupture capping layer, we speculate that this event occurred nearer to ~ 3000 years BP.

Event 7 At the base of the southwestern side of fault F1 we observe a capped fissure and sealed fractures. We do not have age constraint of this event evidence other than it occurred sometime before 2970 ± 230 years BP. Fault F2 in Trench 1 shows additional rupture terminations capped by U50 (dated at 4520 ± 280 years BP). However, we do not have a lower age bound on these events.

We evaluate that there is firm evidence to support at least three surface-rupturing earthquakes in last 3000 years BP with the possibility of four others. Events 2,

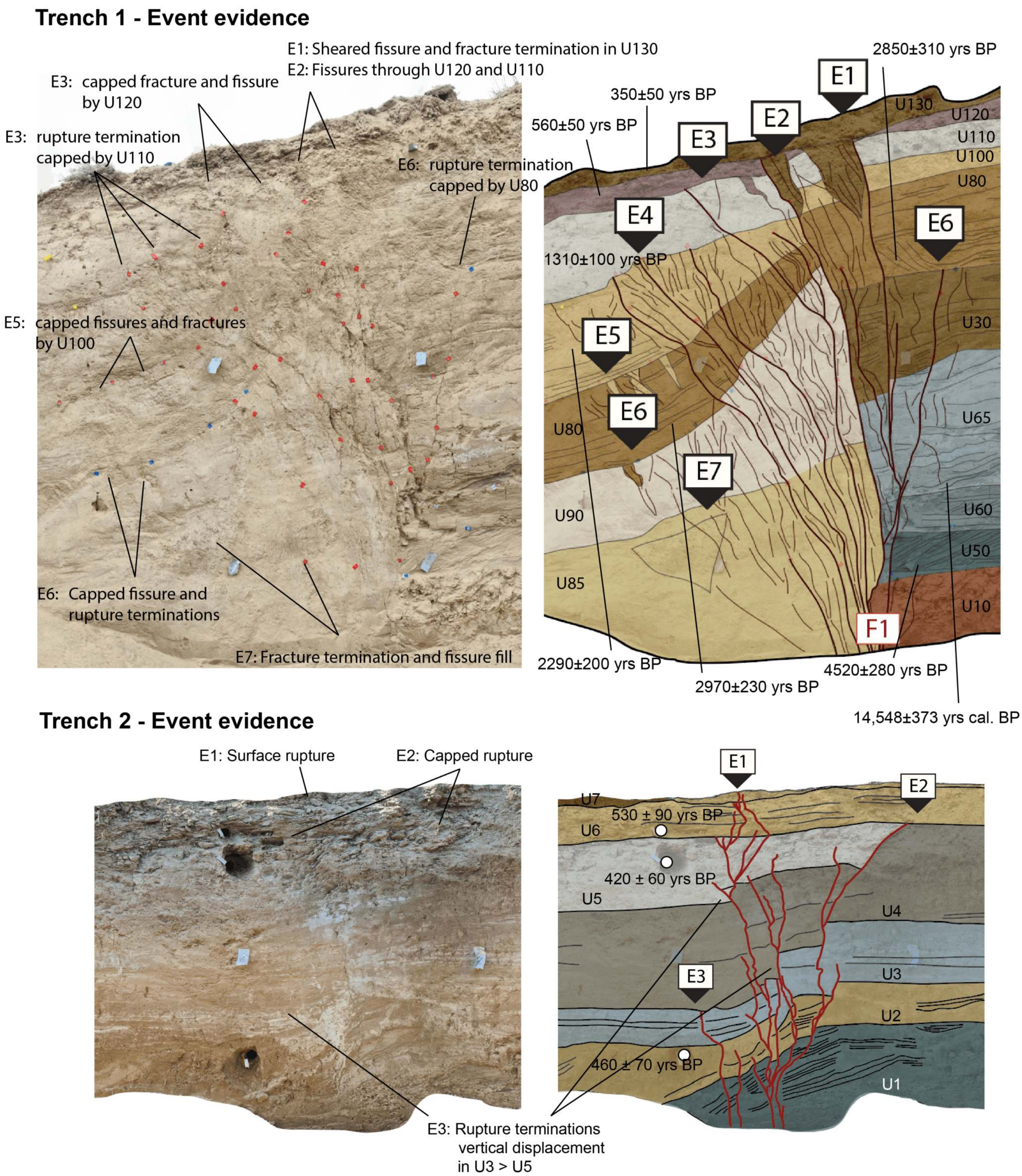

Figure 9 Event evidence from Trenches 1 and 2. Units and event labels are consistent with the trench logs in Fig. 7 & 8. Trench 1 has evidence for at least 4 and up to 7 events. Ages are from IRSL and radiocarbon dating techniques (Tables S1 & S2).

3, and 6 provide the most compelling evidence for co-seismic rupture, given the large fissures and upwards terminating ruptures. These features are unlikely to have formed otherwise. Events 1 and 4 could have formed due to aseismic slip processes rather than earthquakes, as evidenced by upwards termination of rupture, sheared sediments, and a lack of fissuring. Events 5 and 7 are even less confidently identified as earthquakes, as evidenced by capped fissures and fractures with no clearly tracible fault rupture or vertical offset. Additionally, we did not identify colluvial wedges in either trench, which also could suggest aseismic processes. However, the fine-grained nature of the sedimentation and lack of soil development make it difficult to distinguish colluvium in the trench exposure. There are between three and six earthquakes in the last 3000 years giving a surface rupturing event every 500–1000 years on average. We exclude Event 7 from the estimate as we are unable to constrain the age of the overlying deposit.

6 Fault displacement and slip rate of the Shirvan fault

6.1 Displacement and slip rate of the Shirvan fault

The preservation of measurable fault displacements is limited along the fault. These measurements could be made in only a few locations where both a) there is sufficient relief across the fault to preserve displaced features and b) there is not destruction of the fault zone by anthropogenic modification. We were able to locate only 20 lateral displacements in total along the entire 60-km-long fault (Fig. 10).

At the Salyan trench site, we measured a 7.5 ± 0.5 m terrace riser offset in the field, which we confirmed by restoring the slope of the terrace riser using the LaDiCaoz program (Fig. 6). The terrace riser marks the boundary between the older Qt3 and younger Qt1 terraces. At the southeastern end of Trench 1, we observe a channel carved into the clay layers that has been filled with U30 sediments. We interpret the base of Qt3 to be the contact between U20 and U30 in Trench 1. The base of this unit is constrained between 2850 ± 310 and 4520 ± 280 years BP (Fig. 7).

Trench 2 was excavated into the upper layers of the Qt1 terrace. From our IRSL results, we constrain the age of the upper layers of Qt1 between 460 ± 70 and 530 ± 90 years BP (Fig. 9). This provides a poor constraint on the terrace riser offset between 530 ± 90 years BP and 4520 ± 280 years BP. Given the fluvial stratigraphy in Trench 1 it is reasonable to use an age of 2850 ± 310 years BP as a rough age for the Qt3 terrace with a measured offset of 7.5 ± 0.5 m. This yields a late-Holocene slip rate of 2.6 ± 0.3 mm/yr, in the range of the estimated geodetic slip rate of 1.9–3.3 mm/yr (Fig. 1c).

From our field and remote observations, we identified three offsets below 5 m and four offsets between 5 and 10 m (including the 7.5-meter displacement at the Salyan trench site). We infer that the offsets below 5 m occurred in the MRE and the 5–10 m offsets represent at least two events

6.2 Latest-Pleistocene slip rate

To determine a longer-term slip rate on the fault we use the 53 ± 4 m right-lateral displacement of a riser between Qad (upper surface) and Qt2 (lower surface) (Fig. 6). Charcoals from a sample pit excavated into the Qad terrace yielded ages of 1744–2099 and 1824–2145 years cal. BP, giving a slip rate of 28 mm/yr if the sample age is representative of the terrace formation age. This slip rate is an order of magnitude higher than what we expect from the geodetic data. The charcoal nodules are within the Qad deposit and therefore we suspect that these were either deposited with the aeolian sediment or from an anthropogenic source. We also dated a marine shell from the present-day surface of Qad at ~35 ka, which yields a slip rate of less than 2 mm/yr. However, we cannot be certain of the source of the sample as these were not extracted from the logged stratigraphy, and we note that shells can be reworked from other older deposits. Therefore, these slip rate estimates are unreliable.

The last major highstand in the Caspian Sea is thought to be between 11,000–13,500 cal BP, with levels reaching an elevation of 0 m (Arslanov et al., 2016; Dolukhanov et al., 2010; Kakroodi et al., 2012; Kroonenberg et al., 1997; Pánek et al., 2016), which would have submerged the trench site in about 15 m of water. We assume that geomorphic surfaces pre-dating this last highstand would have been reset, such that all fluvial incision and terrace formation must postdate the last highstand. At the last highstand, the marine terrace (Qmt) was formed and as sea level dropped incision began constructing a series of fluvial deposits. During this period active faulting and lateral displacements offset the terraces. If the 53 ± 4 m offset of the terrace riser started to accumulate at a maximum of 11,000–13,500 cal. BP it allows us to infer a minimum geologic slip-rate between 3.6–5.2 mm/yr. This is higher than our late-Holocene slip rate of 2.6 ± 0.3 mm/yr. It is possible that 53 ± 4 m offset riser is exaggerated by fluvial processes after formation, which would imply that the latest-Pleistocene slip rate is overestimated and is an explanation for the different slip rates over different timescales.

6.3 Earthquake recurrence

The estimated recurrence interval, assuming no aseismic slip, from Trench 1 and 2 of 500–1000 years is based on 3 to 6 events in 3000 years. If the earthquake recurrence has remained consistent since the latest-Pleistocene, the ~53 m riser offset over 13,500 years could have been produced by 23–27 earthquakes. This provides a slip per event of 2–3 m to accumulate a 53 m offset, which is consistent with the smallest offset drainages we measured on the Shirvan fault. If we also consider the 7.5 m offset riser, displaced over ~3000 years and assuming the same slip per event of 2–3 m, we get a recurrence interval of 750–1000 years. However, because a substantial portion of this slip may have accumulated aseismically, we cannot draw robust conclusions about coseismic slip-per-event.

7 Discussion

From GNSS measurements, we estimate that the geodetic right-lateral shear totals 1.9 mm/yr on the West Caspian Fault zone (Fig. 1). We have determined a minimum Holocene/latest-Pleistocene slip rate of 3.6–5.2 mm/yr for the Shirvan strand of West Caspian Fault, about double the dextral geodetic rate. Geodetic measurements are limited by relatively few GNSS stations in the Kura Basin. Therefore, the estimated geodetic rate includes an estimated 7.2 mm/yr component of shortening that is accommodated by the Talesh thrust. Furthermore, the geodetic measurements have been made for a relatively short period of time and may not reflect variability in fault slip rates over thousand-year time scales. The 7.5 ± 0.5 m offset terrace riser at the Salyan trench site yields a late-Holocene slip rate of 2.6 ± 0.3 mm/yr, which is comparable with the estimated geodetic rate. This implies that either fluvial erosion has exaggerated the ~54 m offset, or the slip rate on this fault varies through time.

We have mapped the Shirvan fault in detail for a length of more than 60 km (Fig. 3). Linear trends in seismicity and mud volcano alignments suggest that the fault reaches 150 km in length, stretching at least 30 km offshore to the south, and merging northwards with the Greater Caucasus (Fig. 1 and 2), in agreement with the mapping of Zelenin et al. (2022). If the entire 150 km fault were to rupture in an earthquake, log-linear scaling relationships for strike-slip faults in Wesnousky (2008) suggest a maximum slip of 5.9 m and an average slip of 3.0 m. From these displacements we calculate a maximum moment-magnitude of 7.5. The displacements are consistent with the smallest among the limited number of stream offset measurements that we have collected along the fault (Fig. 10). An important result from our Quaternary dating is that although the average recurrence interval is 500–1000 years, the slip events are far from even in timing and show an apparent clustering of two or three events within the last 500 years. However, there are few historical records of large magnitude earthquakes attributed to this area (Ambraseys and Melville, 2005).

Relative relocation of seismicity between 2015 to 2018 (Gunnels et al., 2020) and the ISC-GEM catalogue (Di Giacomo et al., 2018; Storchak et al., 2013, 2015) show shallow seismicity along the fault zone, but with no event larger than M_w6. The pre-instrumentational earthquake catalogue shows no large events within the Salyan-Shirvan region since 3000 BCE (Ambraseys and Melville, 2005), which conflicts with evidence for earthquake clustering over the last 500 years. It is feasible that the absence of major historical earthquakes results from a lack of documentation in this area due to its remoteness or an incomplete historical archive. Alternatively, it is possible that the absence of recorded large earthquakes is real, with the surface ruptures resulting from aseismic processes, lower magnitude earthquakes, or secondary slip events.

Aseismic slip in the West Caspian Fault zone is plausible, as it cuts through ~15 km thickness of sediments of the Kura basin, with high fluid pressures and overpressure demonstrated through active mud volcanism. However, the sedimentation and structure are suggestive of punctuated fault movement in at least a few discrete events, with successive sediment packages capping discrete fracture zones. Another possibility is that there is continuous creep and punctuated sedimentation events create the appearance of discrete slip events in the trench. The slip events seen in our trenches may result from triggered aseismic slip in discrete events, either during fluid mobilization events, or by deeper earthquakes within the basement beneath the Kura basin (Fig. 1 & 2). The 1983 M_w5.8 Kum Dag earthquake, in the Caspian lowlands of Turkmenistan, is a possible analogy for this type of behaviour (e.g. Jackson et al., 2002). This moderate magnitude earthquake had a hypocentral depth of 27 km and yet created a 20 km-long surface rupture and maximum dextral slip of 0.5 m (Trifonov et al., 1986). The surface slip following the Kum Dag earthquake is inferred to have been aseismic and triggered by the deep moderate-magnitude earthquake in the underlying basement. Physical factors such as lithology, sedimentary overpressure, and pore fluid pressure can lead to aseismic slip on faults (e.g., Harris, 2017). Examples of aseismic creep on the Philippine Fault (Leyte Island) correlation to higher fluid pressures in a hydrothermal system (Dianala et al., 2020).

Mud volcanism is a surface phenomenon that occurs in zones of high pore pressure believed to be derived from overpressure, natural gases, and tectonic compressive forces (Mazzini and Etiope, 2017). Compressive tectonic stresses acting on sediments increase pore pressure, create favourable conditions for eruptions, and control mud volcano emplacement. In compressional regions such as the Greater Caucasus and Indonesia, mud volcanoes are found along the top of anticlines with subsurface pathways controlled by the regional stress field (Bonini, 2012). The relationship between strike-slip faulting and mud volcano emplacement is widespread. Examples include the South Coast and Central Range Faults in Trinidad-Tobago (Deville and Guerlais, 2009; Dia et al., 1999; Weber et al., 2020), in the Gulf of Cadiz offshore Spain (Hensen et al., 2015), on the Watukosek fault in Indonesia (Mazzini et al., 2009), and at the southern Salton Sea in California (Onderdonk et al., 2011). These examples suggest that vertically dipping strike-slip faults provide a structural control on mud volcano emplacement. Additionally, where faults bend localised compressive stresses cause folding (Cunningham and Mann, 2007). We observe that mud volcanoes are aligned along active strike-slip faults and appear to be particularly clustered at fault bends (Fig. 2b). We speculate that strike-slip faults and folding from fault bends are controlling the emplacement of mud volcanoes.

8 Conclusion

The West Caspian Fault zone consists of several fault strands and segments that accommodate right-lateral motion on the boundary of Kura and South Caspian basins. From a combination of field observations and satellite remote sensing data we conclude that surface deformation is indicative of right-lateral strike-slip faulting on multiple fault strands. We find geomorphic evidence for surface rupturing earthquakes in the West Caspian fault zone during the last 3000 years. Paleoseismic evidence from the Shirvan fault reveals 3 to 6 surface rupturing earthquakes in the last 3000 years, with a recurrence interval of 500 to 1000 years. At least two of these events occurred within the last 500 years, suggesting a possible cluster of earthquakes. We estimate a minimum geologic slip rate of 3.6–5.2 mm/yr

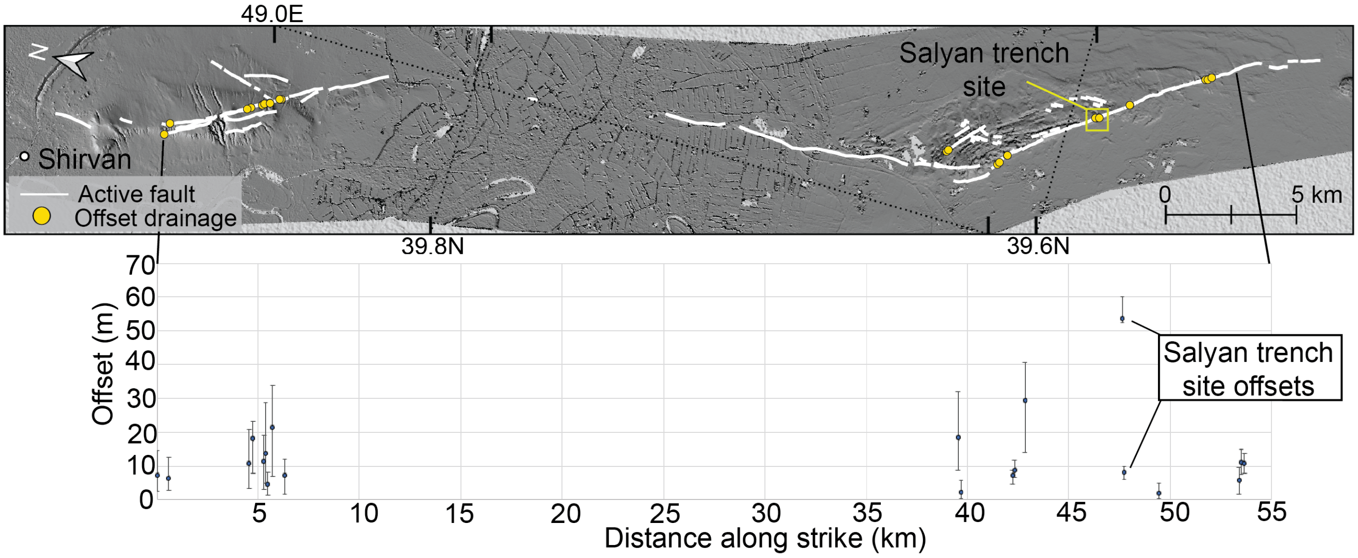

Figure 10 Pléiades stereo-derived digital elevation model of the Shirvan and Salyan sections of the Shirvan fault. On-fault offset drainage measurements are shown by the yellow circles; white lines show the surface fault traces. Offset amounts have been measured remotely (except at the Salyan trench site) and minimum and maximum amounts are measured using the method described in Kurtz et al. (2018).

since the latest-Pleistocene, based on a marine terrace of assumed age. However, this remains uncertain with a lower estimated latest-Holocene slip rate of 1.6–2.7 mm/yrs. Mud volcanism appears to align with active faulting in the West Caspian Fault zone and we find that the Shirvan fault is at least 150 km in length. The presence of mud volcanism, indicative of basin sediment over-pressure combined with tectonic compression could create favourable conditions for aseismic deformation. This could explain the absence of large earthquakes in historical records.

Fault activity in the late Holocene suggests that this fault zone presents a significant seismic hazard for the region and population centers in Azerbaijan.

Acknowledgements

We thank the Republican Seismic Survey, Azerbaijan, for their continued collaborative support. We also thank BP Azerbaijan. The paper was aided through discussions with Prof Rich Koehler, Dr Gordon Seitz, and Prof James Jackson. Satellite imagery was obtained through the Committee for Earth Observing Satellites (CEOS) Seismic Hazards Demonstrator and through funding from St. Edmund Hall, Oxford. Our work was funded through BP Azerbaijan, CASP through a fieldwork award to Neill Marshall, through the NERC-funded COMET (GA/13/M/031), the NERC-ESRC Increasing Resilience to Natural Hazards program "Earthquakes without Frontiers" (NE/J02001X/1), allocation 0009090 from the Research England GCRF Support Fund, and the Leverhulme Trust through research grants EROICA (RPG-2018-371) and NEPTUNE (RPG-2018-243). We would also like to thank the reviewers and editor of this article for their feedback, comments, and contribution.

Data and Code Availability

Point cloud data from both the satellite and UAV photogrammetry processing results is available on the OpenTopography website at https://portal.opentopography.org/dataCatalog, 19/05/2021, SO21034807-2.

No bespoke codes or scripts were written or used to produce this research. The software packages used are referenced in the methods section and includes Microsoft Excel, Agisoft Metashape Pro, and QGIS.

Competing interests

The authors have no competing interests.

References

Abdullayev, N. A., Kadirov, F., and Guliyev, I. S. Subsidence history and basin-fill evolution in the South Caspian Basin from geophysical mapping, flexural backstripping, forward lithospheric modelling and gravity modelling. *Geological Society, London, Special Publications*, 427(1):175–196, 2017. doi: 10.1144/sp427.5.

Allen, M., Jackson, J., and Walker, R. Late Cenozoic reorganization of the Arabia-Eurasia collision and the comparison of short-term and long-term deformation rates. *Tectonics*, 23(2), Mar. 2004. doi: 10.1029/2003tc001530.

Allen, M. B., Jones, S., Ismail-Zadeh, A., Simmons, M., and Anderson, L. Onset of subduction as the cause of rapid Pliocene-Quaternary subsidence in the South Caspian basin. *Geology*, 30(9):775, 2002. doi: 10.1130/0091-7613(2002)030<0775:oosatc>2.0.co;2.

Ambraseys, N. and Melville, C. *A history of Persian earthquakes*. Cambridge University Press, 2005.

Arslanov, K., Yanina, T., Chepalyga, A., Svitoch, A., Makshaev, R., Maksimov, F., Chernov, S., Tertychniy, N., and Starikova, A. On the age of the Khvalynian deposits of the Caspian Sea coasts according to 14C and 230Th/234U methods. *Quaternary International*, 409, 2016. doi: 10.1016/j.quaint.2015.05.067.

Aziz Zanjani, A., Ghods, A., Sobouti, F., Bergman, E., Mortezanejad, G., Priestley, K., Madanipour, S., and Rezaeian, M. Seismicity in the western coast of the South Caspian Basin and the Talesh Mountains. *Geophysical Journal International*, 195(2):799–814, Aug. 2013. doi: 10.1093/gji/ggt299.

Bonini, M. Mud volcanoes: Indicators of stress orientation and tectonic controls. *Earth-Science Reviews*, 115(3):121–152, Nov. 2012. doi: 10.1016/j.earscirev.2012.09.002.

Bronk Ramsey, C. Radiocarbon Calibration and Analysis of Stratigraphy: The OxCal Program. *Radiocarbon*, 37(2):425–430, 1995. doi: 10.1017/s0033822200030903.

Copley, A. and Jackson, J. Active tectonics of the Turkish-Iranian Plateau. *Tectonics*, 25(6), Dec. 2006. doi: 10.1029/2005tc001906.

Cunningham, W. D. and Mann, P. Tectonics of strike-slip restraining and releasing bends. *Geological Society, London, Special Publications*, 290(1):1–12, Jan. 2007. doi: 10.1144/sp290.1.

Deville, E. and Guerlais, S.-H. Cyclic activity of mud volcanoes: Evidences from Trinidad (SE Caribbean). *Marine and Petroleum Geology*, 26(9):1681–1691, Nov. 2009. doi: 10.1016/j.marpetgeo.2009.03.002.

Di Giacomo, D., Engdahl, E. R., and Storchak, D. A. The ISC-GEM Earthquake Catalogue (1904–2014): status after the Extension Project. *Earth System Science Data*, 10(4):1877–1899, Oct. 2018. doi: 10.5194/essd-10-1877-2018.

Dia, A., Castrec-Rouelle, M., Boulègue, J., and Comeau, P. Trinidad mud volcanoes: where do the expelled fluids come from? *Geochimica et Cosmochimica Acta*, 63(7-8):1023–1038, Apr. 1999. doi: 10.1016/s0016-7037(98)00309-3.

Dianala, J. D. B., Jolivet, R., Thomas, M. Y., Fukushima, Y., Parsons, B., and Walker, R. The Relationship Between Seismic and Aseismic Slip on the Philippine Fault on Leyte Island: Bayesian Modeling of Fault Slip and Geothermal Subsidence. *Journal of Geophysical Research: Solid Earth*, 125(12), Nov. 2020. doi: 10.1029/2020jb020052.

Djamour, Y., Vernant, P., Bayer, R., Nankali, H. R., Ritz, J.-F., Hinderer, J., Hatam, Y., Luck, B., Le Moigne, N., Sedighi, M., and Khorrami, F. GPS and gravity constraints on continental deformation in the Alborz mountain range, Iran. *Geophysical Journal International*, 183(3):1287–1301, Oct. 2010. doi: 10.1111/j.1365-246x.2010.04811.x.

Dodds, N., Daout, S., Walker, R. T., Begenjev, G., Bezmenov, Y., Mirzin, R., and Parsons, B. Interseismic deformation and strain-partitioning along the Main Köpetdag Fault, Turkmenistan, with Sentinel-1 InSAR time-series. *Geophysical Journal International*, 230(3):1612–1629, Apr. 2022. doi: 10.1093/gji/ggac139.

Dolukhanov, P. M., Chepalyga, A. L., and Lavrentiev, N. V. The Khvalynian transgressions and early human settlement in the Caspian basin. *Quaternary International*, 225(2):152–159, Oct. 2010. doi: 10.1016/j.quaint.2009.10.039.

Engdahl, E. R., Jackson, J. A., Myers, S. C., Bergman, E. A., and Priestley, K. Relocation and assessment of seismicity in the Iran region. *Geophysical Journal International*, 167(2):761–778, Nov. 2006. doi: 10.1111/j.1365-246x.2006.03127.x.

Feyzullayev, A., Tagiyev, M., and Lerche, I. On the Origin of Hydrocarbons in the Main Lower Pliocene Reservoirs of the South Caspian Basin, Azerbaijan. *Energy Exploration & Exploitation*, 33 (1):1–13, Feb. 2015. doi: 10.1260/0144-5987.33.1.1.

Forte, A., Cowgill, E., Bernardin, T., Kreylos, O., and Hamann, B. Late Cenozoic deformation of the Kura fold-thrust belt, southern Greater Caucasus. *Geological Society of America Bulletin*, 122 (3-4):465–486, Oct. 2009. doi: 10.1130/b26464.1.

Forte, A. M. and Cowgill, E. Late Cenozoic base-level variations of the Caspian Sea: A review of its history and proposed driving mechanisms. *Palaeogeography, Palaeoclimatology, Palaeoecology*, 386, 2013. doi: 10.1016/j.palaeo.2013.05.035.

Forte, A. M., Cowgill, E., Murtuzayev, I., Kangarli, T., and Stoica, M. Structural geometries and magnitude of shortening in the eastern Kura fold-thrust belt, Azerbaijan: Implications for the development of the Greater Caucasus Mountains. *Tectonics*, 32(3), 2013. doi: 10.1002/tect.20032.

Galbraith, R. and Green, P. Estimating the component ages in a finite mixture. *International Journal of Radiation Applications and Instrumentation. Part D. Nuclear Tracks and Radiation Measurements*, 17(3):197–206, Jan. 1990. doi: 10.1016/1359-0189(90)90035-v.

Green, T., Abdullayev, N., Hossack, J., Riley, G., and Roberts, A. M. Sedimentation and subsidence in the South Caspian Basin, Azerbaijan. *Geological Society, London, Special Publications*, 312 (1):241–260, Jan. 2009. doi: 10.1144/sp312.12.

Gunnels, M., Yetrimishli, G., Kazimova, S., and Sandvol, E. Seismotectonic evidence for subduction beneath the Eastern Greater Caucasus. *Geophysical Journal International*, 224(3):1825–1834, Nov. 2020. doi: 10.1093/gji/ggaa522.

Haddon, E. K., Amos, C. B., Zielke, O., Jayko, A. S., and Bürgmann, R. Surface slip during large Owens Valley earthquakes. *Geochemistry, Geophysics, Geosystems*, 17(6), 2016. doi: 10.1002/2015gc006033.

Harris, R. A. Large earthquakes and creeping faults. *Reviews of Geophysics*, 55(1):169–198, Mar. 2017. doi: 10.1002/2016rg000539.

Hensen, C., Scholz, F., Nuzzo, M., Valadares, V., Gràcia, E., Terrinha, P., Liebetrau, V., Kaul, N., Silva, S., Martínez-Loriente, S., Bartolome, R., Piñero, E., Magalhães, V. H., Schmidt, M., Weise, S. M., Cunha, M., Hilario, A., Perea, H., Rovelli, L., and Lackschewitz, K. Strike-slip faults mediate the rise of crustal-derived fluids and mud volcanism in the deep sea. *Geology*, 43(4):339–342, Apr. 2015. doi: 10.1130/g36359.1.

Hollingsworth, J., Jackson, J., Walker, R., and Nazari, H. Extrusion tectonics and subduction in the eastern South Caspian region since 10 Ma. *Geology*, 36(10):763, 2008. doi: 10.1130/g25008a.1.

International Seismological Centre. ISC-GEM Earthquake Catalogue [dataset], 2026. doi: 10.31905/d808b825.

Jackson, J. and McKenzie, D. Active tectonics of the Alpine–Himalayan Belt between western Turkey and Pakistan. *Geophysical Journal International*, 77(1):185–264, Apr. 1984. doi: 10.1111/j.1365-246x.1984.tb01931.x.

Jackson, J., Priestley, K., Allen, M., and Berberian, M. Active tectonics of the South Caspian Basin. *Geophysical Journal International*, 148(2):214–245, Feb. 2002. doi: 10.1046/j.1365-246x.2002.01588.x.

Jackson, J., McKenzie, D., and Priestley, K. Relations between earthquake distributions, geological history, tectonics and rheology on the continents. *Philosophical Transactions of the Royal Society A: Mathematical, Physical and Engineering Sciences*, 379 (2193):20190412, Feb. 2021. doi: 10.1098/rsta.2019.0412.

Kadirov, F., Floyd, M., Alizadeh, A., Guliev, I., Reilinger, R., Kuleli, S., King, R., and Nafi Toksoz, M. Kinematics of the eastern Caucasus near Baku, Azerbaijan. *Natural Hazards*, 63(2):997–1006, Apr. 2012. doi: 10.1007/s11069-012-0199-0.

Kakroodi, A., Kroonenberg, S., Hoogendoorn, R., Mohammd Khani, H., Yamani, M., Ghassemi, M., and Lahijani, H. Rapid Holocene sea-level changes along the Iranian Caspian coast. *Quaternary International*, 263, 2012. doi: 10.1016/j.quaint.2011.12.021.

Karney, C. GeographicLib (Version 1.51) [software], 2019. https:

//Geographiclib.Sourceforge.Io/1.51.

Khain, V., Grigoryants, B., and Isayev, B. The West Caspian Fault and factors governing the formation of transverse faults in geosynclinal fold belts. *MOIP Bulletin*, 41, 1966.

Khorrami, F., Vernant, P., Masson, F., Nilfouroushan, F., Mousavi, Z., Nankali, H., Saadat, S. A., Walpersdorf, A., Hosseini, S., Tavakoli, P., Aghamohammadi, A., and Alijanzade, M. An up-to-date crustal deformation map of Iran using integrated campaign-mode and permanent GPS velocities. *Geophysical Journal International*, 217(2):832–843, Jan. 2019. doi: 10.1093/gji/ggz045.

Kroonenberg, S., Rusakov, G., and Svitoch, A. The wandering of the Volga delta: a response to rapid Caspian sea-level change. *Sedimentary Geology*, 107(3-4):189–209, Jan. 1997. doi: 10.1016/s0037-0738(96)00028-0.

Kroonenberg, S., Abdurakhmanov, G., Badyukova, E., van der Borg, K., Kalashnikov, A., Kasimov, N., Rychagov, G., Svitoch, A., Vonhof, H., and Wesselingh, F. Solar-forced 2600 BP and Little Ice Age highstands of the Caspian Sea. *Quaternary International*, 173-174:137–143, Oct. 2007. doi: 10.1016/j.quaint.2007.03.010.

Kurtz, R., Klinger, Y., Ferry, M., and Ritz, J.-F. Horizontal surface-slip distribution through several seismic cycles: The Eastern Bogd fault, Gobi-Altai, Mongolia. *Tectonophysics*, 734-735, 2018. doi: 10.1016/j.tecto.2018.03.011.

Leroy, S. A. G., Lahijani, H. A. K., Crétaux, J.-F., Aladin, N. V., and Plotnikov, I. S. *Past and Current Changes in the Largest Lake of the World: The Caspian Sea*, page 65–107. Springer International Publishing, 2020. doi: 10.1007/978-3-030-42254-7_3.

Mangino, S. and Priestley, K. The crustal structure of the southern Caspian region. *Geophysical Journal International*, 133(3), 1998. doi: 10.1046/j.1365-246x.1998.00520.x.

Mazzini, A. and Etiope, G. Mud volcanism: An updated review. *Earth-Science Reviews*, 168:81–112, May 2017. doi: 10.1016/j.earscirev.2017.03.001.

Mazzini, A., Nermoen, A., Krotkiewski, M., Podladchikov, Y., Planke, S., and Svensen, H. Strike-slip faulting as a trigger mechanism for overpressure release through piercement structures. Implications for the Lusi mud volcano, Indonesia. *Marine and Petroleum Geology*, 26(9):1751–1765, Nov. 2009. doi: 10.1016/j.marpetgeo.2009.03.001.

McCaplin, J. *Paleoseismology*, volume 95. Academic Press, 2nd edition, 2009.

Nadirov, R., Bagirov, E., Tagiyev, M., and Lerche, I. Flexural plate subsidence, sedimentation rates, and structural development of the super-deep South Caspian Basin. *Marine and Petroleum Geology*, 14(4), 1997. doi: 10.1016/s0264-8172(96)00054-2.

NASA SRTM. NASA Shuttle Radar Topography Mission (SRTM) Global [dataset], 2013. doi: 10.5069/G9445JDF.

Ollivier, V., Fontugne, M., Lyonnet, B., and Chataigner, C. Base level changes, river avulsions and Holocene human settlement dynamics in the Caspian Sea area (middle Kura valley, South Caucasus). *Quaternary International*, 395:79–94, Feb. 2016. doi: 10.1016/j.quaint.2015.03.017.

Onderdonk, N., Mazzini, A., Shafer, L., and Svensen, H. Controls on the geomorphic expression and evolution of gryphons, pools, and caldera features at hydrothermal seeps in the Salton Sea Geothermal Field, southern California. *Geomorphology*, 130(3-4), 2011. doi: 10.1016/j.geomorph.2011.04.014.

Pierce, I. and Koehler, R. 3D Paleoseismology from iOS Lidar and Structure from Motion Photogrammetry: a case study on the Dog Valley fault, California. *Seismica*, 2(1), Jan. 2023. doi: 10.26443/seismica.v2i1.208.

Pierce, I., Guliyev, I., Yetirmishli, G., Muradov, R., Kazimova, S., Javanshir, R., De Pascale, G. P., Johnson, B., Marshall, N., Walker, R., and Wordsworth, P. Surface Rupturing Earthquakes of the Greater Caucasus Frontal Thrusts, Azerbaijan. *Tectonics*, 43(3), Mar. 2024. doi: 10.1029/2023tc007758.

Piip, V. B., Rodnikov, A. G., and Buvaev, N. A. The deep structure of the lithosphere along the Caucasus-South Caspian Basin-Apsheron Threshold-Middle-Caspian Basin-Turan plate seismic profile. *Moscow University Geology Bulletin*, 67(2):125–132, Mar. 2012. doi: 10.3103/s0145875212020068.

Pánek, T., Korup, O., Minár, J., and Hradecký, J. Giant landslides and highstands of the Caspian Sea. *Geology*, 44(11):939–942, Nov. 2016. doi: 10.1130/g38259.1.

Reilinger, R., McClusky, S., Vernant, P., Lawrence, S., Ergintav, S., Cakmak, R., Ozener, H., Kadirov, F., Guliev, I., Stepanyan, R., Nadariya, M., Hahubia, G., Mahmoud, S., Sakr, K., ArRajehi, A., Paradissis, D., Al-Aydrus, A., Prilepin, M., Guseva, T., Evren, E., Dmitrotsa, A., Filikov, S. V., Gomez, F., Al-Ghazzi, R., and Karam, G. GPS constraints on continental deformation in the Africa-Arabia-Eurasia continental collision zone and implications for the dynamics of plate interactions. *Journal of Geophysical Research: Solid Earth*, 111(B5), May 2006. doi: 10.1029/2005jb004051.

Rhodes, E. J. Dating sediments using potassium feldspar single-grain IRSL: Initial methodological considerations. *Quaternary International*, 362:14–22, Mar. 2015. doi: 10.1016/j.quaint.2014.12.012.

Shebalin, N. and Leydecker, G. *Earthquake Catalogue for the Former Soviet Union and Borders up to 1988*. European Commission, 1997.

Storchak, D., Di Giacomo, D., Engdahl, E., Harris, J., Bondár, I., Lee, W., Bormann, P., and Villaseñor, A. The ISC-GEM Global Instrumental Earthquake Catalogue (1900–2009): Introduction. *Physics of the Earth and Planetary Interiors*, 239:48–63, Feb. 2015. doi: 10.1016/j.pepi.2014.06.009.

Storchak, D. A., Di Giacomo, D., Bondar, I., Engdahl, E. R., Harris, J., Lee, W. H. K., Villasenor, A., and Bormann, P. Public Release of the ISC-GEM Global Instrumental Earthquake Catalogue (1900-2009). *Seismological Research Letters*, 84(5), 2013. doi: 10.1785/0220130034.

Trifonov, V. G., Vostrikov, G. A., Lykov, V. I., Orazsakhatov, K., and Skobelev, S. F. Tectonic Aspects of the 1983 Kum-Dag Earthquake, West Turkmenia. *International Geology Review*, 28(4): 377–389, Apr. 1986. doi: 10.1080/00206818609466278.

Vernant, P., Nilforoushan, F., Hatzfeld, D., Abbassi, M. R., Vigny, C., Masson, F., Nankali, H., Martinod, J., Ashtiani, A., Bayer, R., Tavakoli, F., and Chéry, J. Present-day crustal deformation and plate kinematics in the Middle East constrained by GPS measurements in Iran and northern Oman. *Geophysical Journal International*, 157(1):381–398, Apr. 2004. doi: 10.1111/j.1365-246x.2004.02222.x.

Walker, R. T., Bezmenov, Y., Begenjev, G., Carolin, S., Dodds, N., Gruetzner, C., Jackson, J. A., Mirzin, R., Mousavi, Z., and Rhodes, E. J. Slip-Rate on the Main Köpetdag (Kopeh Dagh) Strike-Slip Fault, Turkmenistan, and the Active Tectonics of the South Caspian. *Tectonics*, 40(8), Aug. 2021. doi: 10.1029/2021tc006846.

Weber, J., Geirsson, H., La Femina, P., Robertson, R., Churches, C., Shaw, K., Latchman, J., Higgins, M., and Miller, K. Fault Creep and Strain Partitioning in Trinidad-Tobago: Geodetic Measurements, Models, and Origin of Creep. *Tectonics*, 39(1), Jan. 2020. doi: 10.1029/2019tc005530.

Wesnousky, S. G. Displacement and Geometrical Characteristics of Earthquake Surface Ruptures: Issues and Implications for Seismic-Hazard Analysis and the Process of Earthquake Rupture. *Bulletin of the Seismological Society of America*, 98(4):

1609–1632, Aug. 2008. doi: 10.1785/0120070111.

Zelenin, E., Bachmanov, D., Garipova, S., Trifonov, V., and Kozhurin, A. The Active Faults of Eurasia Database (AFEAD): the ontology and design behind the continental-scale dataset. *Earth System Science Data*, 14(10):4489–4503, Oct. 2022. doi: 10.5194/essd-14-4489-2022.

Zhang, H., Aldana-Jague, E., Clapuyt, F., Wilken, F., Vanacker, V., and Van Oost, K. Evaluating the potential of post-processing kinematic (PPK) georeferencing for UAV-based structure- from-motion (SfM) photogrammetry and surface change detection. *Earth Surface Dynamics*, 7(3), 2019. doi: 10.5194/esurf-7-807-2019.

Zielke, O. and Arrowsmith, R. LaDiCaoz and LiDARimager—MATLAB GUIs for LiDAR data handling and lateral displacement measurement. *Geosphere*, 8(1):206, 2012. doi: 10.1130/ges00686.1.